Disentangling initial-state and evolution effects in heavy-ion collisions using EPOS and PHSD

Mahbobeh Jafarpour,[1,*] Vadym Voronyuk,[2] Klaus Werner,[1,†] Elena Bratkovskaya,[3,4,5] and Damien Vintache[1]

[1]*SUBATECH, University of Nantes–IN2P3/CNRS–IMT Atlantique, Nantes, France*

[2]*Joint Institute for Nuclear Research, Joliot-Curie 6, 141980 Dubna, Moscow region, Russia*

[3]*GSI Helmholtzzentrum für Schwerionenforschung GmbH, Planckstrasse 1, D-64291 Darmstadt, Germany*

[4]*Institut für Theoretische Physik, Johann Wolfgang Goethe-Universität, Max-von-Laue-Strasse 1, D-60438 Frankfurt am Main, Germany*

[5]*Helmholtz Research Academy Hesse for FAIR (HFHF), GSI Helmholtz Center for Heavy-Ion Physics, Campus Frankfurt, 60438 Frankfurt, Germany*

(Received 5 September 2025; accepted 24 December 2025; published 21 January 2026)

In this study we examine the impact of the initial stage and dynamical evolution on final-state observables in heavy-ion collisions. For this goal we develop a novel approach, EPOSir + PHSDe, which employs energy-conserving multiple parallel scattering approach, accommodating factorization and saturation (EPOS) initial conditions as the starting point for parton and hadron evolution within the parton-hadron-string dynamics (PHSD) microscopic transport approach. By examining the space-time evolution of matter in this model and comparing to EPOS (which starts with an *S*-matrix approach for parallel scatterings for the initial conditions and uses a hydrodynamic evolution for the quark-gluon plasma stage with the UrQMD as afterburner) and PHSD (which starts with primary high-energy *NN* scattering realized via the LUND string model and continues with fully microscopic transport dynamics for strongly interacting partonic and hadronic matter), we identify the key differences in the final particle distributions among the three approaches. Our analysis focuses on rapidity, transverse momentum spectra, and flow harmonics v_2 for Au + Au collisions at the invariant energy of $\sqrt{s_{NN}} = 200$ GeV. We find a dominant influence of dynamical evolution over the initial conditions on the final observables.

DOI: 10.1103/k41y-p793

I. INTRODUCTION

Ultrarelativistic heavy-ion collisions (HICs) at RHIC and LHC create a hot, ultradense state of deconfined quarks and gluons, known as the quark-gluon plasma (QGP) [1–5]. Experimental and theoretical studies seek to characterize the QGP, understand its formation, and explore its evolution and observable signatures. HICs involve multiple stages, typically divided into an initial preequilibrium phase (for $t < 1$ fm/c) and a subsequent evolution phase covering expansion, thermalization, and hadronization. Various model approaches introduce different assumptions that have an impact on experimental interpretations.

Despite significant progress uncertainties remain, particularly in understanding thermalization and the transition from an out-of-equilibrium state to a thermalized QGP. The first phase involves the energy deposition and primary scattering, setting the initial conditions. The second phase includes the nonequilibrium evolution, leading to QGP formation and hydrodynamic expansion. The final stage covers hadronization, followed by a hadronic cascade and freezeout.

Exploring different theoretical models and simulations for these stages is crucial. Several formalisms, including the color glass condensate (CGC) frameworks, classical Yang-Mills dynamics, and transport models, describe the initial stage [6–10]. For the QGP evolution relativistic viscous hydrodynamics effectively models collective flow, while transport and hybrid models bridge partonic and hadronic descriptions. Systematic comparisons of these approaches, validated against experimental data, are a key to advance our understanding of the QGP and the dynamical evolution of the strongly interacting matter.

The goal of our study is to disentangle the impact of the initial-state and the evolution dynamics on final observables in heavy-ion collisions. For that we use EPOS4 (energy-conserving multiple parallel scattering approach, accommodating factorization and saturation) [11–15] (replacing earlier EPOS versions [16–19]) and PHSD (parton-hadron-string dynamics) microscopic approach [20–28]; both models have well-defined "initial" and "evolution" stages:

(1) The initial phase of EPOS (EPOSi) amounts to an *S*-matrix approach for instantaneous parallel scatterings, whereas the following dynamics has been realized so far by assuming that a fast equilibration occurs followed by a hydrodynamical evolution (EPOSe).

*Contact author: mahbobeh.jafarpour@subatech.in2p3.fr

†Contact author: Werner@subatech.in2p3.fr

Published by the American Physical Society under the terms of the Creative Commons Attribution 4.0 International license. Further distribution of this work must maintain attribution to the author(s) and the published article's title, journal citation, and DOI. Funded by SCOAP³.

(2) The PHSD models the initial high-energy nucleon-nucleon scatterings and the string formation based on the LUND string model using the Pythia event generator in the initial phase (PHSDi), whereas the evolution is based on a microscopic covariant dynamical approach for strongly interacting systems using Kadanoff-Baym equations (PHSDe) in the semiclassical limit.

When comparing two models, such as EPOS and PHSD, it is not always straightforward to determine the relative contributions of the initial phase (i) and the expansion phase (e) to the final results. To address this issue, the idea of combining the initial phase from EPOS (EPOSi) with the evolution from PHSD (PHSDe) gave rise to the EPOSir + PHSDe model, where EPOSir adds a rope procedure to EPOSi. This approach allows for a clear comparison between two models based on distinct contributions from the initial conditions and the evolution. By comparing EPOSir + PHSDe to EPOS, we isolate the differences arising from the evolution phase, since both models share identical initial conditions but differ in their time evolution. However, when comparing EPOSir + PHSDe to PHSD, we are comparing models with different initial conditions but the same evolution, allowing us to clearly distinguish between the contributions of the initial conditions and the evolution phase.

In this study we focus on transverse momentum spectra and flow harmonics in Au + Au collisions at the invariant energy $\sqrt{s_{NN}} = 200$ GeV, which is well suited to study the dynamics of strongly interacting matter due to the large volume of the QGP and relatively long life time of the formed fireball such that the system proceeds toward a partial thermalization.

The outline of the paper is as follows: in Sec. II we present the theoretical basis of EPOS and PHSD and the combined new approach, EPOSir + PHSDe. In Sec. III we present and compare the results of the three alternative approaches, EPOS, EPOSir + PHSDe, and PHSD, for various observables of Au + Au collisions at the top RHIC energy, such as bulk matter observables, and anisotropic flows. We summarize our findings in Sec. IV.

II. COMBINED EPOS + PHSD APPROACH

A. EPOS

EPOS (which refers to EPOS4 in this paper) starts with so-called primary scatterings, happening simultaneously at $t = 0$ (EPOSi). It follows a core-corona procedure, an assumed fast equilibration of the core with a subsequent hydrodynamical evolution and microcanonical hadronization, and finally a hadronic cascade (EPOSe). For a detailed description, see Refs. [11–14]; a pedagogical overview can be found in Ref. [15].

EPOSi. The primary scatterings amount to parallel partonic scatterings, happening instantaneously, at $t = 0$. The theoretical tool is S-matrix theory, using a particular form of the multiple scattering S-matrix. Each elementary scattering process is described by Pomeron exchange, a Pomeron being realized as a parton ladder [12]. A very important aspect of EPOS is the treatment of high parton density effects,

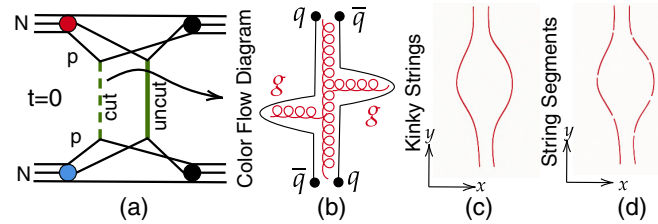


FIG. 1. From Pomerons to string segments: (a) Elementary interactions for a nucleon-nucleon scattering in EPOS, showing a cut Pomeron (dashed green line) and an uncut Pomeron (full green line). (b) Color flow diagram corresponding to a cut ladder. (c) Kinky strings from color flow diagram. (d) String segments.

representing nonlinear parton evolutions, which are accounted for by implementing a dynamical saturation scale, which depends for each Pomeron on its energy, but also the environment (neighboring Pomeons) [13]. The approach is compatible with the current understanding of parton saturation. To evaluate the multiple scattering S-matrix expressions, cutting rule techniques are employed [13], which leads to an expansion of cross-sections in terms of products of cut and uncut Pomerons [sketched in Fig. 1(a)]. A cut Pomeron is considered to be an essentially longitudinal color field in the form of a flux tube, whose dynamics is described by relativistic string theory via so-called kinky strings; see Figs. 1(b) and 1(c). In elementary collisions, the string breaking by quark-antiquark production leads to hadron formation from the individual string segments identified as hadrons; see Fig. 1(d).

To construct "the core," one considers the space-time evolution of these string segments and in particular the intersection of their trajectories with a hyperbola representing a fixed proper time τ. We know not only the space-time position of each segment but also its velocity. In principle, we have a dynamical system, where all elements move, but we may get some estimate of the fate of each segment by considering its trajectory through the matter composed of all the other segments at their fixed position at τ. In this way, we compute the energy loss of each string segment as [14]

$$P_t^{\text{new}} = P_t - f_{\text{Eloss}} \int_\gamma \rho dL, \tag{1}$$

where γ and P_t are the trajectory and transverse momentum of the string segment, respectively. f_{Eloss} is a nonzero constant, and ρ is the local string density. If P_t^{new} is positive, the string segment can escape from the dense area, and it is categorized as a "corona particle." If P_t^{new} is negative, however, the string segment lost all its energy and is unable to leave, thus it will remain in the dense area and is called "core particle." All the core particles constitute "the core."

EPOSe. Here we have to distinguish between the core and the corona particles. The core expands hydrodynamically based on relativistic viscous hydrodynamic equations with shear viscosity to entropy ratio $\eta/s = 0.08$ and zero bulk viscosity [14,19]. The microcanonical method [14] is employed to hadronize the core. The corresponding hadrons, as well as the corona particles (originating directly from string decay)

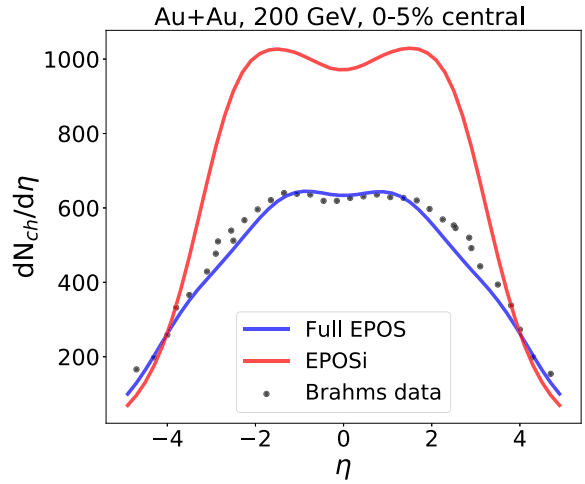


FIG. 2. Charged particle multiplicities ($dN_{\rm ch}/d\eta$) as a function of pseudorapidity (η) in Au + Au collisions at invariant energy 200 GeV for different simulations, Full EPOS (blue curve, including hydro), and EPOSi (red curve, without hydro, without hadronic cascade) for central collisions (0–5%). The experimental data are taken from BRAHMS [30] with black points.

follow straight-line trajectories, but they continue to interact via hadronic scattering, employing the UrQMD model [29].

A full EPOS simulation amounts to both, primary and secondary interactions (EPOSi and EPOSe). But it is interesting to see what we get (concerning particle production) if we consider only EPOSi, assuming that all string segments convert to hadrons. The charged particle multiplicity is shown in Fig. 2 as a function of the pseudorapidity for full EPOS (including hydro) and just EPOSi (without hydro), compared to data from the BRAHMS experiment [30]. Full EPOS (with hydro, blue curve) can reasonably well reproduce the experimental data. However, EPOSi (without hydro, red curve) overestimates the experimental data by a large amount. This shows the essential role of hydrodynamics, which allows to redistribute the system energy from the "mass production" to the kinetic energy of the expanding fireball. To understand the big difference in particle production in the two scenarios, one has to realize that in the hydro case a strong transverse flow develops (which dominates spectra at intermediate values of transverse momenta), and there is also longitudinal work; both features reduce the energy available for particle production, where the latter (per cell) is the energy in the comoving frame of the cell.

B. PHSD

PHSD is a nonequilibrium microscopic transport approach that incorporates both hadronic and partonic degrees of freedom [20–24,27,28]. It provides a comprehensive description of the entire evolution of relativistic heavy-ion collisions, starting from initial out-of-equilibrium nucleon-nucleon (NN) interactions, progressing through the formation and interactions of the quark-gluon plasma, and extending to hadronization and the final-state interactions of produced hadrons.

The dynamical evolution of the system is governed by the Cassing-Juchem generalized off-shell transport equations, formulated within the test-particle representation [31,32]. These equations arise from a first-order gradient expansion of the Kadanoff-Baym equations [33], which effectively describe strongly interacting degrees of freedom [22,34]. For a more detailed discussion, see Ref. [35].

PHSDi. The initial collisions of PHSD are build by the primary independent scattering of the initial nucleons (according to Wood-Saxon distribution) from colliding nuclei. The high-energy NN reactions [as well as elementary baryon-baryon (BB) reactions above $\sqrt{s^{\rm th}_{BB}} = 2.65$ GeV, meson-baryon (mB) collisions above $\sqrt{s^{\rm th}_{mB}} = 2.35$ GeV, and meson-meson (mm) reactions above $\sqrt{s^{\rm th}_{mm}} = 1.3$ GeV] leading to multiparticle production are described by the Lund string model [36]. These are realized through event generators FRITIOF 7.02 [36,37] and PYTHIA 6.4 [38], which are "tuned" for a more accurate description of low and intermediate energy reactions. The "PHSD tune" [39] of the Lund string model modifies string fragmentation and hadron properties in the hot, dense medium of heavy-ion collisions. It incorporates chiral symmetry restoration via the Schwinger mechanism [40,41], accounts for the initial-state Cronin effect in k_T broadening, and implements in-medium hadron properties by using momentum-, density-, and temperature-dependent spectral functions instead of constant-width nonrelativistic ones [42,43]. The color neutral strings decay into leading hadrons and "prehadrons," unformed mesons and baryons from string fragmentation in the Lund model.

PHSDe. The prehadron formation time is $t_F = \tau_F \gamma$, with $\tau_F = 0.8$ fm/c and $\gamma = 1/\sqrt{1 - v^2/c^2}$. Leading hadrons interact immediately with reduced cross-sections [44], while prehadrons remain noninteracting for $t < t_F$ in "cold" matter with energy density $\varepsilon < \varepsilon_C$, where $\varepsilon_C = 0.5$ GeV/fm^3, based on lattice QCD [45]. Below ε_C, prehadrons evolve into hadronic states and interact via hadronic cross-sections.

If $\varepsilon \simeq \varepsilon_C$, prehadrons melt into thermal partons, governed by the dynamical quasiparticle model (DQPM) model. Partonic interactions in the QGP phase are modeled within the effective DQPM model, formulated in the two-particle irreducible (2PI) propagator representation [28,46–48]. The DQPM describes nonperturbative QCD matter in line with the lattice QCD equation-of-state (EoS) at finite temperature T and baryon chemical potential $\mu_{\rm B}$ [49,50]. In this approach, partons are off-shell quasiparticles with complex self-energies: the real part determines a dynamically generated mass, while the imaginary part governs interaction rates, yielding spectral functions with finite widths. The $(T, \mu_{\rm B})$-dependence of self-energies follows a hard-thermal-loop-inspired parametrization, with a single parameter fixed by matching the DQPM entropy density (or pressure/energy density) to lattice QCD results at $\mu_{\rm B} = 0$. The partonic interactions include elastic $2 \leftrightarrow 2$ scatterings ($qq \leftrightarrow qq$, $\bar{q}\bar{q} \leftrightarrow \bar{q}\bar{q}$, $gg \leftrightarrow gg$) and inelastic $2 \leftrightarrow 1$ processes ($gg \leftrightarrow g$, $q\bar{q} \leftrightarrow g$), described by a relativistic Breit–Wigner cross-section. The DQPM framework provides a consistent description of the QCD thermodynamics and the QGP properties in terms of transport coefficients in the whole (T, μ_B) plane [28,48,51–53] as well as a nonequilibrium description—via Kadanoff-Baym equations—of strongly interacting degrees

of freedom propagated in a self-generated scalar mean-field potential [21]. We note that in this study we use the PHSD version 4.1 which is linked to the DQPM model for $\mu_B = 0$, which is a good approximation for the relativistic energies considered here.

As the fireball expands, parton hadronization occurs near the phase boundary between hadronic and partonic matter, which lattice QCD data indicate as a crossover [45]. The hadronic system is then described using off-shell HSD dynamics, optionally incorporating self-energies for hadronic degrees of freedom [42,43,54].

C. Reasoning for combining EPOS + PHSD approaches

As described above, the EPOS and PHSD approaches have fundamentally different initial conditions and matter evolutions; nevertheless, they provide rather similar results in many observables but differences in some others.

To disentangle the influence of the initial-state and evolution effects on the final observables of heavy-ion collisions—which is the aim of this study—we combine the two different approaches in a single framework, called "EPOSir + PHSDe," in which the standard EPOS initial conditions (EPOSi), complemented by a rope procedure (EPOSir), are employed as the starting point for the PHSD-based parton and hadron evolution (PHSDe).

III. DYNAMICS OF HICS WITHIN EPOSIR + PHSDE

A. Initial conditions according to EPOSi

The combined EPOSir + PHSDe approach is based on EPOS initial conditions discussed in Sec. II A. Thus, here we focus only on the issues which are important for the EPOS/PHSD connection.

As the first step, we use the known distribution of nucleons in the initial nuclei (Wood-Saxon in case of heavy nuclei such as Au) to generate nucleon positions for both projectile and target. In EPOSi, an *S*-matrix approach allows for the determination of pairs of interacting nucleons and the corresponding Pomerons. Interacting nucleons are referred to as participants, the other ones are called spectators. The participants are mainly within the overlap zone, which is a theoretical construction representing the overlap of two spheres; see Fig. 3. The Pomerons are identified by parton ladders. Following the color flow, one constructs chains of partons (COP), which can be mapped to kinky strings. Two integer numbers will characterize the different "objects," referred to as "status" (ist) and "type" (ity). The first one allows differentiating between Pomerons, parton chains, and string segments, whereas the latter one gives additional information, like being core or corona particle. The whole picture, namely, interactions via Pomerons, identification of chains of partons, kinky strings, and string segments, is sketched in Fig. 4.

Technically, the method consists of three steps: first, the Pomerons produce several COPs, then they are converted to kinky strings (S), and finally, the strings are split into several string segments, as discussed in the EPOSi part. In Fig. 5, we show the corresponding space-time picture. We show for simplicity a situation where we have just two strings (one in blue, the other one in red). The red and blue points close to the x axis represent the locations of the string origins. Starting at these points, the strings evolve (here we sketch simple yo-yo strings) and then break. The trajectories of the string segments (also referred to as prehadrons) are indicated as dashed lines (red and blue from the two different strings). We indicate as dots the intersections of the string segment trajectories with

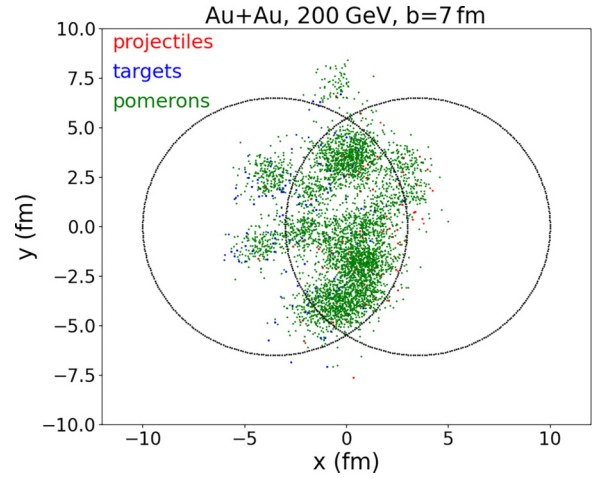


FIG. 3. Positions in the transverse plane of the projectile (red points) and target (blue points) participants and their corresponding Pomerons. We consider here 20 semiperipheral Au + Au collisions at the invariant energy $\sqrt{s_{NN}} = 200$ GeV.

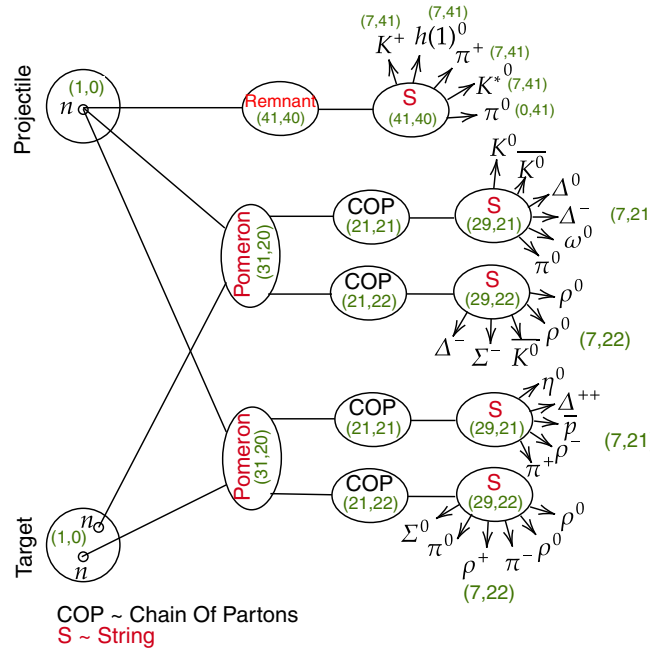


FIG. 4. Sketch of initialization in EPOSi based on the multiple Pomeron exchange. Pomerons represent the interactions between nucleons from the projectile and the target. The Pomerons convert into several chains of partons (COP), and then the COP is split into string segments. The first and second numbers in parentheses represent the particle's status (ist) and type (ity) [55].

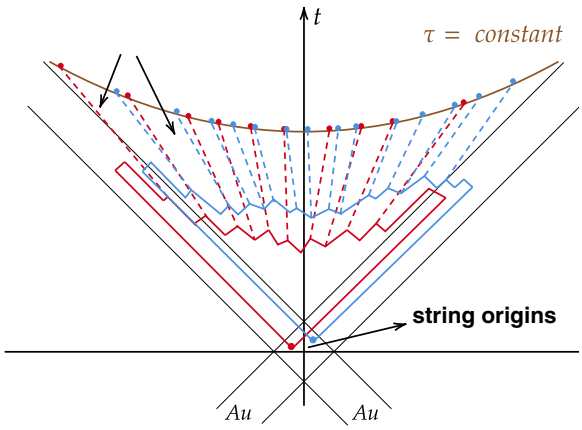


FIG. 5. Space-time picture of the string segment production (see text).

a hyperbola corresponding to some proper time τ. At the same time, we have projectile and target remnants that decay into several "prehadrons." For simplicity, we show only the projectile remnant in Fig. 4.

The prehadrons may be very close to each other, this is why in EPOS a core-corona procedure is employed. In EPOS, the core segments define the initial condition for a hydrodynamical evolution. The string segments are shown in three dimensions, i.e., transverse plane versus longitudinal direction z in Fig. 6(a), employing the space-time rapidity η_s instead of z for the longitudinal dimension, being defined as $\eta_s = \frac{1}{2}\log((t+z)(t-z))$.

Figure 6(a) depicts the string segments at a given τ. The core segments are presented as colored (blue and red) objects. For simplicity, only flat strings are shown. It is also possible (but not shown) to have corona particles in the middle of the core segments, if their kinetic energy is large enough.

B. EPOSir: EPOSi + ropes

In EPOS + PHSD, we also use this core-corona picture. Having identified the core, we have to transform it into an initial condition of PHSD, which requires "prehadrons." Naively, one may directly use all the "EPOS prehadrons" as prehadrons for PHSD. But this turned out not to work at all, the multiplicity will be much too high. So we modify EPOSi by introducing ropes, referred to as "EPOSi+ropes" or simply EPOS4ir. We consider connected areas of the core as "ropes," which generally defines objects obtained from fusing strings. This is essentially what we do with the core construction. All the other string segments (those not contributing to the ropes) are referred to as corona particles. We sketch the "rope production" in Fig. 6(b).

We point out that using EPOSi leads to the production of many prehadrons and, consequently, to a strong overestimation of the final hadron yield (roughly twice as many as in experiments), when employing PHSDe. As discussed earlier, this "overproduction" is compensated by the hydro evolution, which helps to convert the energy stored in the masses into flow and work. The introduction of the ropes, i.e., the method "EPOSi+ropes" (EPOSir in short), decreases the number of

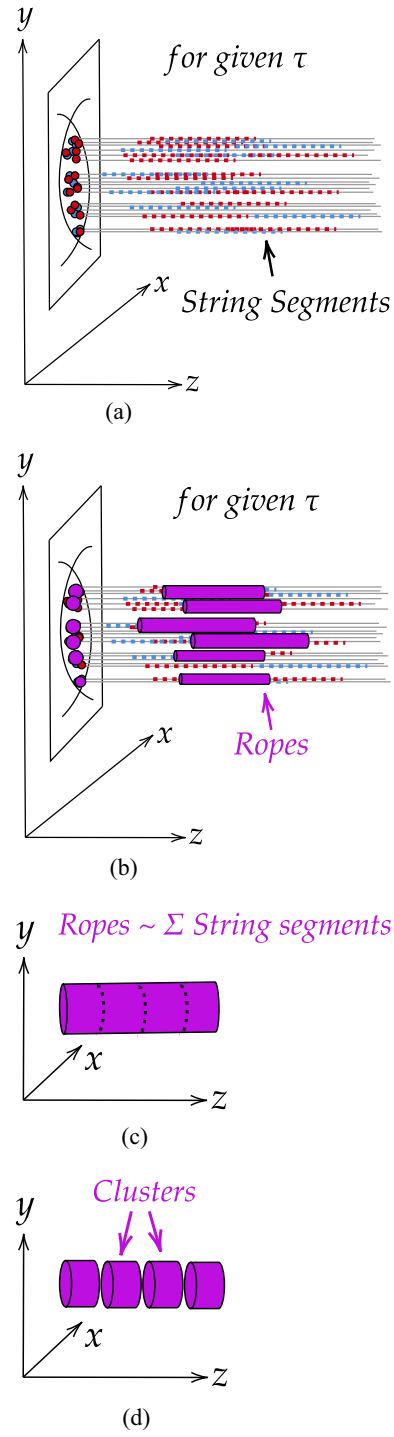


FIG. 6. From string segments (prehadrons) to cluster formation in three dimensions at given τ. (a) String segments production. (b) Overlapping string segments defining the rope segments. (c) Constructing the rope segment. (d) Cutting the rope segment into disks (clusters).

prehadrons (per unit of pseudorapidity), as shown in Fig. 7 for central Au + Au collisions at $\sqrt{s_{NN}} = 200$ GeV. Thus, the ropes allow to convert the initial large mass production in the Pomeron picture in EPOS to the kinetic energy of degrees-of-freedom.

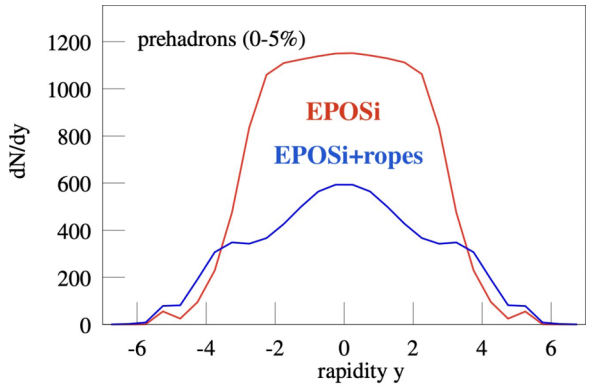


FIG. 7. Initial stage rapidity distributions of prehadrons for EPOSi (red curve) and EPOSi+ropes (=EPOSir, blue curve) in most central 0–5% Au + Au collisions at $\sqrt{s_{NN}} = 200$ GeV averaged over 5000 events.

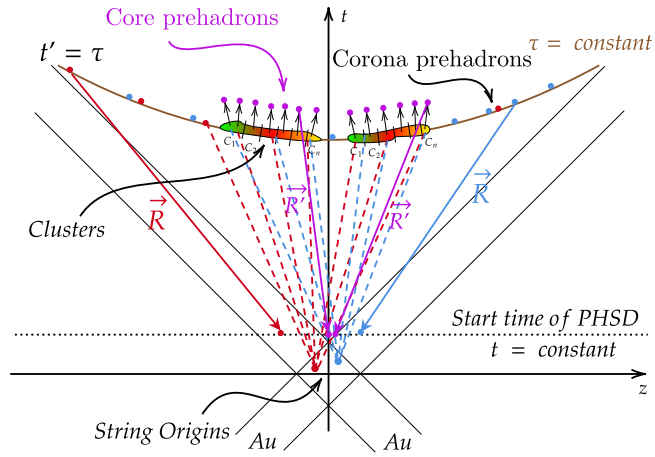


FIG. 8. Extrapolation back-in-time procedure of core and corona prehadrons to the starting time of PHSD.

Ropes are considered as longitudinal color fields similar to ordinary strings. We then break the rope segments into several pieces, called "clusters," for technical reasons, as illustrated in Fig. 6(c).

Technically, we employ a cluster algorithm, based on a cell-centered grid in three dimensions, which enables us to define slices in the longitudinal variable and identify connected transverse areas and the corresponding transverse density distribution. These connected sections in transverse space amount to rope slices, or clusters, as illustrated in Fig. 6(d).

These rope slices (or clusters) are not static, but they are assumed to have a transverse flow profile (resulting in higher transverse momenta of its decay products) and have a longitudinal flow profile (resulting in a broader rapidity distribution). Both effects will reduce the particle multiplicity of particles from cluster decay.

To prepare the evolution for PHSD, we will decay the clusters into hadrons, using the usual EPOS procedure of microcanonical decay of an object of mass M (with flow profiles) in its center of mass, with a subsequent boost back into the laboratory system. The technical details can be found in Ref. [14]. In EPOSir + PHSDe language, we call these hadrons "rope core prehadrons" (they have hadron properties, but are not final state hadrons yet).

The prehadronization is realized slice by slice, where different slices correspond to different values of η_s. There is a strong correlation between η_s and the rapidity y of the rope segment, in the sense that the rapidity of the cluster is essentially equal to η_s. Therefore, the core prehadrons produced from the decay of a rope slice at given η_s show up at y close to η_s.

The sequence of clusters corresponds to a sequence of η_s values (in an ordered fashion) and correspondingly the clusters are sitting at different values of rapidity (again ordered), so the final rapidity distribution of prehadrons will be a sum of many (Gaussian-like) peaks, adding up to a broad (essentially flat) distribution.

To avoid possible confusion, let us recall the definitions of the different core prehadrons: those produced in the EPOS core-corona procedure are called "EPOS core prehadrons," which are the basis of the production of ropes and clusters. The latter decay, and the decay products are called "rope core prehadrons," because they are produced from rope decay. So at this stage, we have "corona prehadrons" and "rope core prehadrons."

The ropes in our approach are identical to the ropes used in many other approaches (PYTHIA for example), in the sense that they are considered to be longitudinal color fields similar to ordinary strings, but with modified decay properties. But in practice, there are many ways to create and decay ropes. In the case of PYTHIA, the rope is created by adding color representations, and the decay is kind of the inverse procedure, where the breaks occur string by string, with an effective string tension being the difference $\kappa_{p,q} - \kappa_{p-1,q}$. The value of $\kappa_{p,q}$ is proportional to the Casimir operator of the corresponding representation. The procedure in EPOS is completely different. It is based on string segments (from cutting strings into pieces), where string theory tells us what the four momenta of these objects (called prehadrons) are. The core-corona procedure is based on the energy loss of prehadrons when traversing the "matter" made by all other prehadrons. In this way, we get core prehadrons, being those which lose all their energy. Then we identify connected areas of prehadrons, which define our ropes. For the decay, we use microcanonical hadronization, representing the maximum of the entropy.

C. Inserting prehadrons into PHSD

On the one hand, EPOS operates with Milne coordinates, and thereby the prehadrons are produced on a hyperbola in space-time. On the other hand, the PHSD code uses the cartesian coordinates (x, y, z) at a given time t. The knowledge of the space distribution of energy and baryon densities is crucial for PHSD dynamics. Therefore one has to appoint some relation between the two coordinate systems. In principle, we just need to extrapolate the prehadrons from the hyperbola back to the constant timeline, see Fig. 8. Since the positions, time, and momenta are known, then we know the trajectories:

$$\vec{R}(t) = \vec{R}(t_p) + \vec{V}_p \times (t - t_p), \tag{2}$$

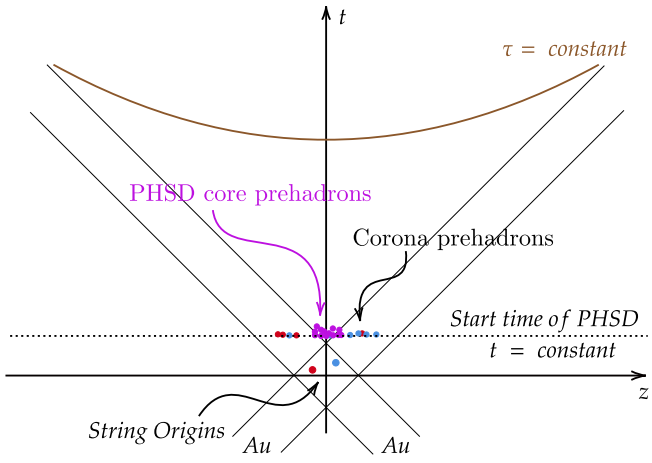


FIG. 9. Schematic depiction of the final places of PHSD core prehadrons and the corona prehadrons after extrapolation and melting at the start time of the PHSD evolution.

where $\vec{R}(t_p)$ in the position of the particle at time t_p, V_p – its velocity. Thereby, one can compute the position at the initial time in PHSD ($t = t_{\mathrm{ini_{PHSD}}}$). This is actually what is done for "corona prehadrons." They can be immediately inserted into PHSD. We call this procedure "normal extrapolation," which can be seen by red and blue arrows in Fig. 8. We note that in PHSD the inserted prehadrons become formed hadrons after passing the formation time t_F as discussed in Sec. II B. Concerning the "rope core prehadrons," the situation is more complicated, since these "prehadrons" did not exist prior to the hyperbola line, but what exists are their "parents." The cluster decay particles (rope core prehadrons) are placed at the corresponding time at the positions of string segments having produced the clusters. These segments are referred to as "parents" with respect to the clusters, whereas the decay products (rope core prehadrons) are referred to as "children." All the string segments contributing to cluster formation are "EPOS core prehadrons." This nontrivial extrapolation procedure, namely, placing the children (with their momenta) at the position of the parents, see the violet arrows in Fig. 8, assures an accurate energy density distribution at any PHSD time step. The extrapolated children are referred to as "PHSD core prehadrons."

The evolution of partonic and hadronic phases in PHSD is governed by the local energy density calculated on the space grid at each time step. The original algorithm was extended to include "parents" and "corona prehadrons." If the average energy density exceeds the critical energy density (0.5 GeV/fm^3), the corresponding PHSD core prehadrons must be melted before their formation into the partonic phase. This is called the "melting procedure." Note that the corona prehadrons do not melt into the partonic phase but contribute to the energy density.

Figure 9 shows a schematic picture of the final positions of core and corona prehadrons following the extrapolation and melting processes to the PHSD start time. For the energy under consideration almost all of the prehadrons are melted during the first few PHSD time steps but for low energies, the process can be stretched in time. The rest of the evolution of matter is carried out using the PHSD nonequilibrium dynamics once all prehadrons have been inserted into PHSD arrays. In the following subsection, we will discuss the space-time evolution of particles in EPOSir + PHSDe.

D. Space-time evolution of HICs in EPOSir + PHSDe

PHSD employs a space-time grid that expands in time to describe HICs. Since the particle density is high at the initial stage of the PHSD evolution, a considerable number of interactions occur. Therefore, the time step must be short enough to consider their interactions reasonably. The system expands later, and the size of the cells steadily rises. In the axis parallel to the beam direction (generally referred to as the z axis), the PHSD grids are expanded with time to cover the whole system on the grid.

Following the melting condition, the PHSD core prehadrons become deconfined into partons at a time of 0.064 fm/c. This number corresponds to $t_{\mathrm{ini_{PHSD}}} + \Delta t$, with $t_{\mathrm{ini_{PHSD}}} = R/\gamma$ being the PHSD start time (the time just after the two nuclei passed through each other). It happens that after the first time step, i.e., at $t_{\mathrm{ini_{PHSD}}} + \Delta t$, the prehadrons become deconfined, simply because the conditons are fulfilled. The partonic phase begins at this time.

The partonic phase evolves in time until the system is cooling due to the expansion. Then the hadronization occurs dynamically for the quarks/antiquarks entering in the cells with a local energy density below the critical one. The quarks/antiquarks fuse into mesons or (anti)baryons according to the transition rate [21]. In parallel, the number of mesons (baryons) rises with time due to hadronization, and they spread in space, resulting in blue (green) points.

E. Momentum eccentricity

To understand better the dynamical observables of the bulk matter, we investigate here the time evolution of the momentum eccentricity for three models—EPOS, PHSD, and EPOSir + PHSDe—which shows how the pressure gradients develop in time.

The momentum eccentricity of each cell is defined as

$$\epsilon_p = \frac{\sum \varepsilon\, v^2 \cos(2\phi)}{\sum \varepsilon\, v^2}, \tag{3}$$

where $v^2 = v_x^2 + v_y^2$ is the transverse hydrodynamic velocity of the cell, $\phi = \arctan(v_y/v_x)$ the azimuthal angle, and ε the energy density of the cell. The hydrodynamical velocity is defined as $u^\mu T_{\mu\nu} = \varepsilon u_\nu$, where $T_{\mu\nu}$ is the energy-momentum tensor; the eigenvector u^μ is the four-velocity ($v = u/u^0$). To compute the energy density in EPOS, we use the energy-momentum tensor $T^{\mu\nu}$, which is at the start time given by [14]

$$T^{\mu\nu}(x) = \sum_i \frac{p_i^\mu p_i^\nu}{p_i^0} g(x - x_i), \tag{4}$$

where x is the space-time, p_i the four-momentum of the prehadron i, x_i its space-time, and g a Gaussian smoothing kernel [see Eq. (5) of Ref. [14]]. The energy density is given as T^{00}

in the comoving frame. This is the way one determines the energy density in EPOS, more precisely by solving $u^\mu T_{\mu\nu} = \varepsilon u_\nu$. This is used as initial condition for hydro. Then the hydro module takes over, and computes step by step (among others) the energy density on a space grid.

In both EPOSir + PHSDe and PHSD, the energy density for each cell in the global computational frame—which is conventionally selected as the initial $N + N$ (nucleon-nucleon) center-of-mass frame—is defined as [56]

$$\varepsilon = \frac{\sum_i E_i}{V_{\text{cell}}}, \tag{5}$$

where the sum of all particles in the cell is provided by $\sum_i$, and the volume of the cell is defined by $V_{\text{cell}} = \Delta x \Delta y \Delta z$ where $\Delta x = \Delta y = 1$ fm which is equal to the hadron size and Δz is time-dependent and adjusted dynamically as $\Delta z = 1/\gamma_{\text{cm}}$ fm for $t < t_0$ and $\Delta z = 1/\gamma_{\text{cm}} + (t - t_0)c$ fm for $t \geqslant t_0$, where t_0 is the touching time of the two colliding nuclei. Here $\gamma_{\text{cm}} = \sqrt{s_{NN}}/(2m_N)$, s_{NN} is the invariant energy of the N + N system.

The local energy density for each cell in the rest frame of the cell is computed using the velocity of this cell:

$$\vec{\beta} = \frac{\sum_i \vec{p}_i}{\sum_i E_i}, \tag{6}$$

which gives the Lorentz factor $\gamma = 1/\sqrt{1 - \vec{\beta}^2}$. Therefore, the local energy density of the cells is determined by

$$\varepsilon' = \frac{E'}{V'} = \frac{E/\gamma}{V \times \gamma} = \frac{\varepsilon}{\gamma^2}. \tag{7}$$

In Fig. 10 we show the momentum eccentricity ϵ_P for semiperipheral Au + Au collisions at the invariant energy $\sqrt{s_{NN}} = 200$ GeV for the three models. The momentum eccentricity in EPOS using hydro with the default value (see Sec. II A and Refs. [14,19]) of the shear viscosity to entropy ratio $\eta/s = 0.08$ (top left panel) strongly increases on average (thick line) with time, but with large fluctuations for individual events (thin lines): some of these lines grow very strongly, beyond values of 0.7, and others show a modest increase. This spread is a consequence of the large fluctuations in the initial shape: sometimes an elongated shape is produced, and sometimes it is completely symmetric. The former leads to a strong asymmetric flow due to hydrodynamic pressure and a strong increase in the momentum eccentricity. The latter leads to a small asymmetric flow and a modest increase in momentum eccentricity. Since elongated shapes are produced frequently, they affect the average curve considerably, and one gets the observed strong increase of the average momentum eccentricity with time.

We show as well the EPOS result for $\eta/s = 0.24$ (the top right panel), where the average curve grows somewhat less than the one for the $\eta/s = 0.08$ case. Also the fluctuations are less pronounced.

The PHSD and EPOSir+PHSDe momentum eccentricities are shown in the middle left and middle right panels of Fig. 10 while the lower panel shows the comparison of the averaged ϵ_P for all models. One can see that the momentum eccentricity in the PHSD model fluctuates much less than the

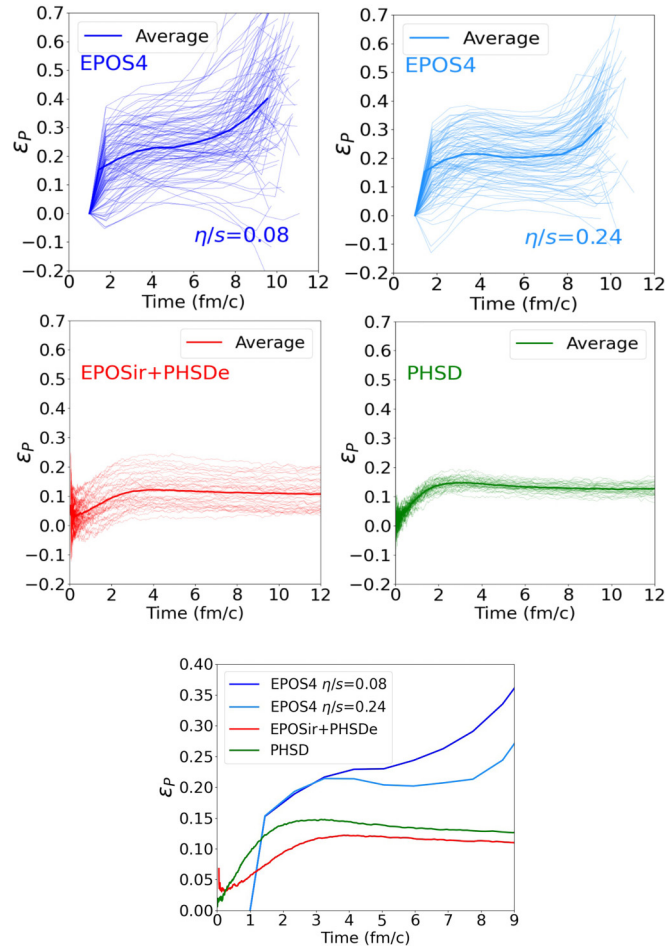


FIG. 10. Momentum eccentricity (ϵ_P) as a function of time for EPOS with $\eta/s = 0.08$ (top left), EPOS with $\eta/s = 0.24$ (top right), PHSD (middle right), EPOSir + PHSDe (middle left) calculated for 100 EPOS events, 800 EPOSir + PHSDe and 800 PHSD events of Au + Au collisions at $\sqrt{s_{NN}} = 200$ GeV with an impact parameter $b = 7$ fm, as well as a comparison of the averaged values of ϵ_P (bottom).

EPOS one, it grows rapidly and saturates after 2 fm/c. The initial EPOSir conditions lead to stronger fluctuations of ϵ_P in case of EPOSir + PHSDe, however, the PHSD dynamical evolution takes over and leads to a saturation of the ϵ_P approximately at the same averaged value as for the PHSD.

This comparison shows that the "evolution," i.e., realization of the partonic and hadronic interactions during the expansion, is more important than the "initial conditions" for the building of pressure. Indeed, starting with identical initial conditions for EPOSir + PHSDe and EPOS, we obtain a saturation of ϵ_P for EPOSir + PHSDe and a monotonic increase of ϵ_P for the EPOS. But we should always keep in mind that we cannot use directly EPOSi as initial condition for PHSDe, but we need to add the rope procedure (→ EPOSir).

The strongly increasing ϵ_P has consequences on final observables: in EPOS, a strong asymmetric flow is associated to a strong radial flow; the latter is visible in the p_T spectra (dN/dp_T) at intermediate p_T (1–4 GeV/c), the former in the

p_T dependence of v_2 (we note that turning off the flow, both dN/dp_T and $v_2(p_T)$ would drop significantly).

IV. BULK MATTER OBSERVABLES

In this section we present and compare the results from the three models—EPOS, PHSD and EPOSir + PHSDe—for the bulk matter observables such as the rapidity and pseudorapidity densities, transverse momentum spectra, transverse mass spectra, and anisotropic flow coefficients for Au + Au collisions at invariant energy $\sqrt{s_{NN}} = 200$ GeV. Moreover, we confront our calculations with corresponding experimental data from the BRAHMS, PHENIX, PHOBOS, and STAR collaborations.

A. Rapidity and pseudorapidity distributions

We start with showing the pseudorapidity distributions of charged hadrons. In Fig. 11, we present the EPOS (top panel), EPOSir + PHSDe (middle panel), and PHSD (lower panel) results for the pseudorapidity distributions of charged hadrons from most central (0–5%) to semiperipheral (40–50%) Au + Au collisions at $\sqrt{s_{NN}} = 200$ GeV in comparison to the BRAHMS data [30]. One can see that the PHSD describes the BRAHMS data very well for all centrality classes with the same shape as the experiment. EPOS approximately reproduces the experimental data, however, the η-distribution from EPOS is more narrow than the data for all centrality bins. EPOSir + PHSDe produces slightly more charged particles at midpseudorapidity, however, it can well reproduce experimental data for semiperipheral collisions.

In Fig. 12, we present the rapidity densities for identified charged particles [$\pi^{\pm}$ (red curves), $K^{\pm}$ (blue curves), p (red curves), $\bar{p}$ (blue curves), and net proton $p - \bar{p}$ (red curves)] from EPOS (left panel), EPOSir + PHSDe (middle panel), and PHSD (right panel) for most central (0–5%) Au + Au collision at the invariant energy $\sqrt{s_{NN}} = 200$ GeV. The theoretical calculations (integrated over all p_T) are compared to the BRAHMS data [57,58] and shown for two cases: including the weak decays (dashed lines) or not (solid lines). This concerns pions, where weak decays of K_S play an important role, and protons, where Λ decays are significant.

The first two rows of Fig. 12 represent the $\pi^{\pm}$ (red curves) and $K^{\pm}$ (blue curves) rapidity densities. In all simulations, pions and kaons are a bit above the experimental data. One can see that the rapidity distributions for light mesons from all three models are slightly broader than the experimental data contrary to the results for the charged particle distributions shown in Fig. 11 where the model η-distributions are consistent with the data or even narrower than the data.

The rapidity distributions of protons (red curves), antiprotons (blue curves), and net-protons are shown in the third and fourth rows of Fig. 12. Whereas the experimental proton and antiproton rapidity densities decrease with rapidity, the net-proton density grows. The simulations show a similar trend. Concerning weak decays, the situation is not clear from the experimental side. The data are not feed-down corrected, but from the detector design, we do not expect weak decay products to contribute considerably. So the data are in reality

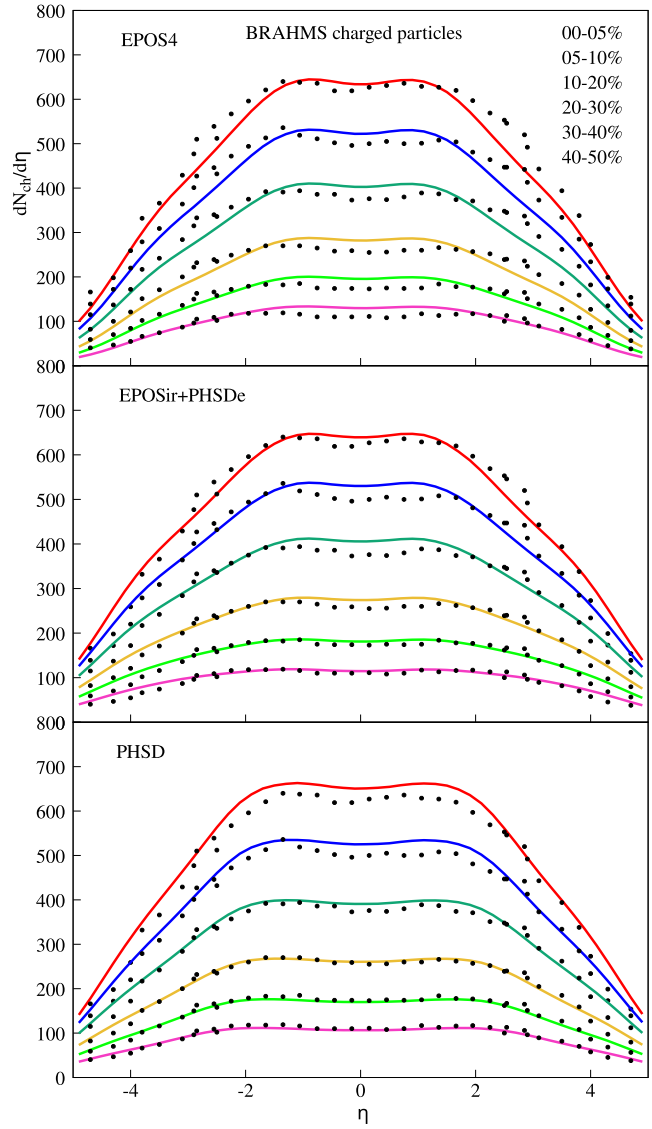


FIG. 11. Charged particle distribution ($dN_{\rm ch}/d\eta$) as a function of pseudorapidity (η) for Au + Au collisions at $\sqrt{s_{NN}} = 200$ GeV for EPOS (top panel), EPOSir + PHSDe (middle panel), and PHSD (lower panel) from central to semiperipheral collisions (from top to bottom: 0–5%, 5–10%, 10–20%, 20–30%, 30–40%, and 40–50%). The experimental data (black dots) are taken from the BRAHMS collaboration [30].

between "feed-down corrected" and "all feed-down included." If we consider the average of the net-proton results with and without the contribution of weak decays, then we find that EPOSir + PHSDe produces results that are closer to the real data than EPOS and PHSD. In PHSD, the proton, antiproton, and net-proton distributions with or without weak decay contribution are slightly higher than EPOS and EPOSir + PHSDe in forward rapidity ($3 < y < 5$).

B. Transverse mass spectra

In Figs. 13, 14, and 15, we present the transverse mass ($m_T = \sqrt{p_T^2 + m^2}$) spectra for charged pions ($\pi^{\pm}$), charged

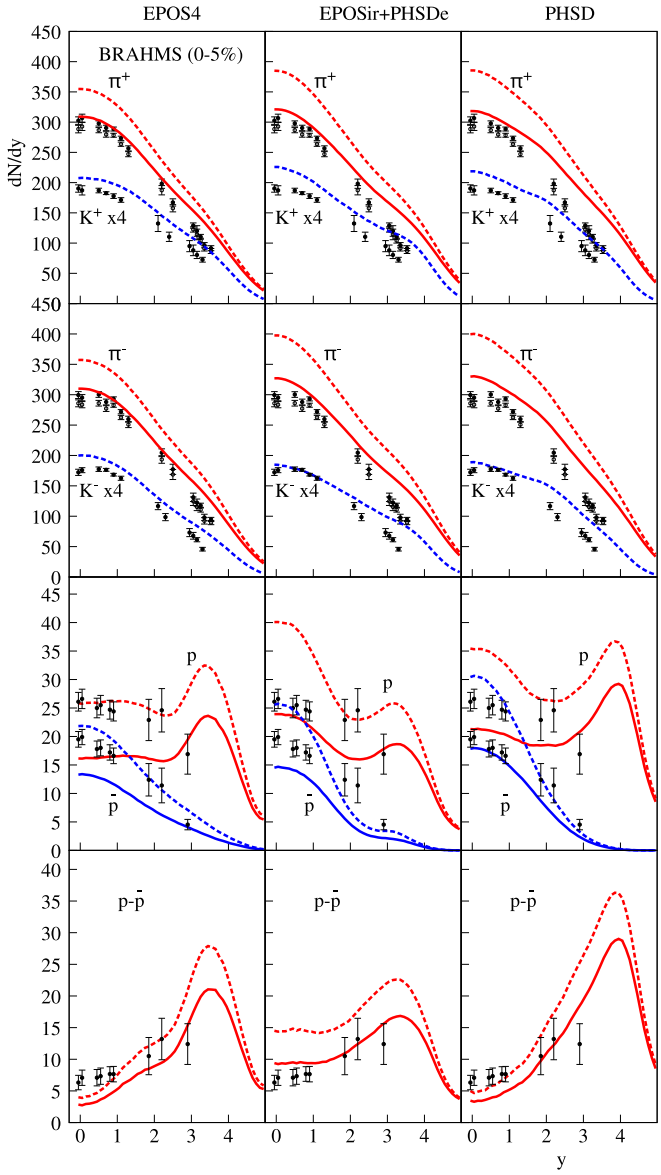


FIG. 12. Rapidity distributions of (from top to bottom) π^+ (red curves) and K^+ (blue), π^- (red) and K^- (blue), p (red) and $\bar{p}$ (blue), and net protons $p-\bar{p}$ (red) for the 5% most central Au + Au collisions at $\sqrt{s_{NN}} = 200$ GeV, from EPOS (left panel), EPOSir + PHSDe (middle panel), and PHSD (right panel). The solid lines indicate the results without weak decays, while the dashed lines refer to results containing weak decay products. The kaon yields were multiplied by 4 for clarity. The black dots indicate the BRAHMS data [57,58] without weak decay corrections (in case of pions also with).

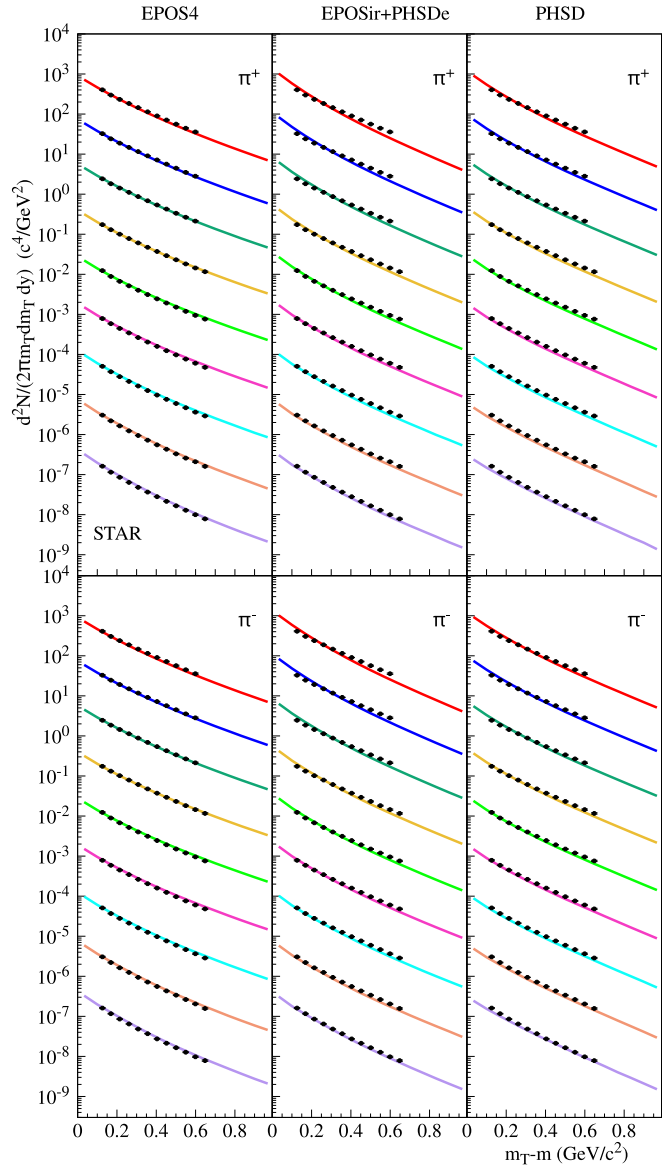


FIG. 13. Invariant yield as a function of transverse mass for π^+ and π^- in Au + Au collision at $\sqrt{s_{NN}} = 200$ GeV at midrapidity ($|y| < 0.5$) for EPOS (left panel), EPOSir + PHSDe (middle panel) and PHSD (right panel). The m_T spectra are plotted for different centrality bins, from top to bottom: 0–5%, 5–10%, 10–20%, 20–30%, 30–40%, 40–50%, 50–60%, 60–70%, 70–80%, in each plot. The results are compared to the STAR experimental data [59] (black dots). All curves and experimental data are scaled by 10^{-n} starting from the top curve with 10^0.

kaons ($K^{\pm}$), as well as protons (p) and antiprotons ($\bar{p}$), respectively, for Au + Au collision at $\sqrt{s_{NN}} = 200$ GeV for the three models in comparison to STAR data [59]. We show results for nine centrality classes, i.e. (from top to bottom for each plot), 0–5%, 5–10%, 10–20%, 20–30%, 30–40%, 40–50%, 50–60%, 60–70%, 70–80%.

As seen from Figs. 13 and 14 all three models can reproduce well the experimental results for all centrality classes in the case of pions ($\pi^{\pm}$) and kaons/antikaons ($K^{\pm}$). The results from EPOSir + PHSDe (middle panel) are quite similar to PHSD (right panel) and EPOS (left panel).

However, the m_T spectra for the p and $\bar{p}$ show model deviations: as follows from Fig. 15, EPOS reproduces the STAR data for all centrality classes while EPOSir + PHSDe and PHSD show a slightly steeper slope compared to the data and EPOS, respectively.

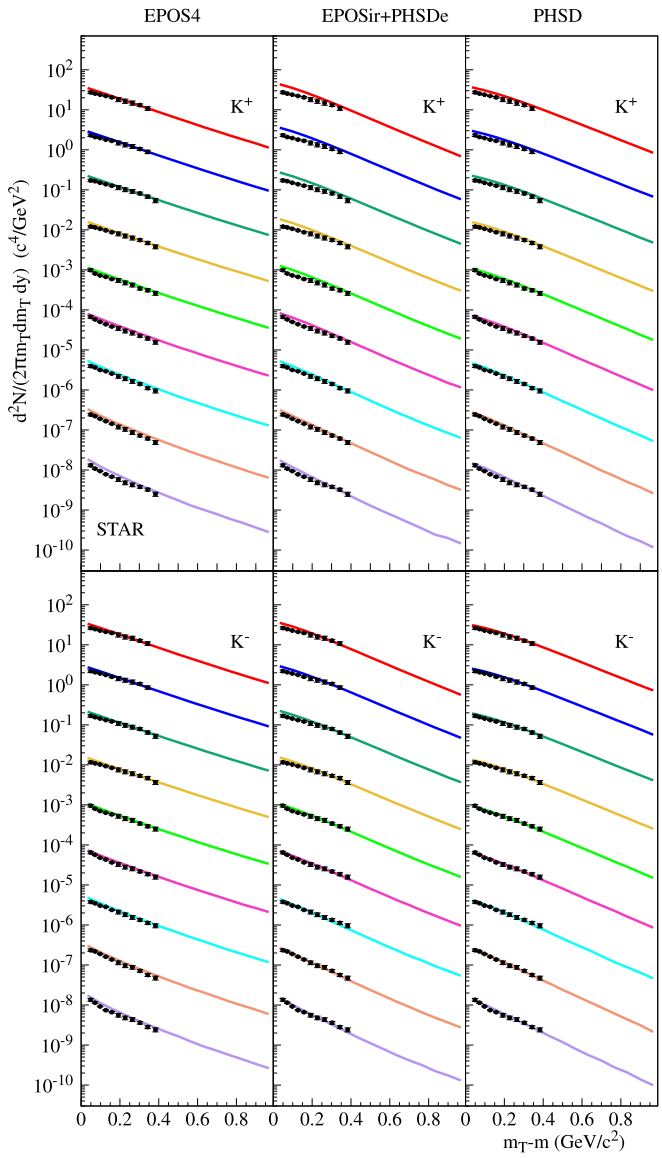


FIG. 14. Invariant yield as a function of transverse mass for K^+ and K^- in Au + Au collision at $\sqrt{s_{NN}} = 200$ GeV at midrapidity ($|y| < 0.5$) for EPOS (left panel), EPOSir + PHSDe (middle panel) and PHSD (right panel). The m_T spectra are plotted for different centrality bins, from top to bottom: 0–5%, 5–10%, 10–20%, 20–30%, 30–40%, 40–50%, 50–60%, 60–70%, 70–80%, in each plot. The results are compared to the STAR experimental data [59] (black dots). All curves and experimental data are scaled by 10^{-n} starting from the top curve with 10^0.

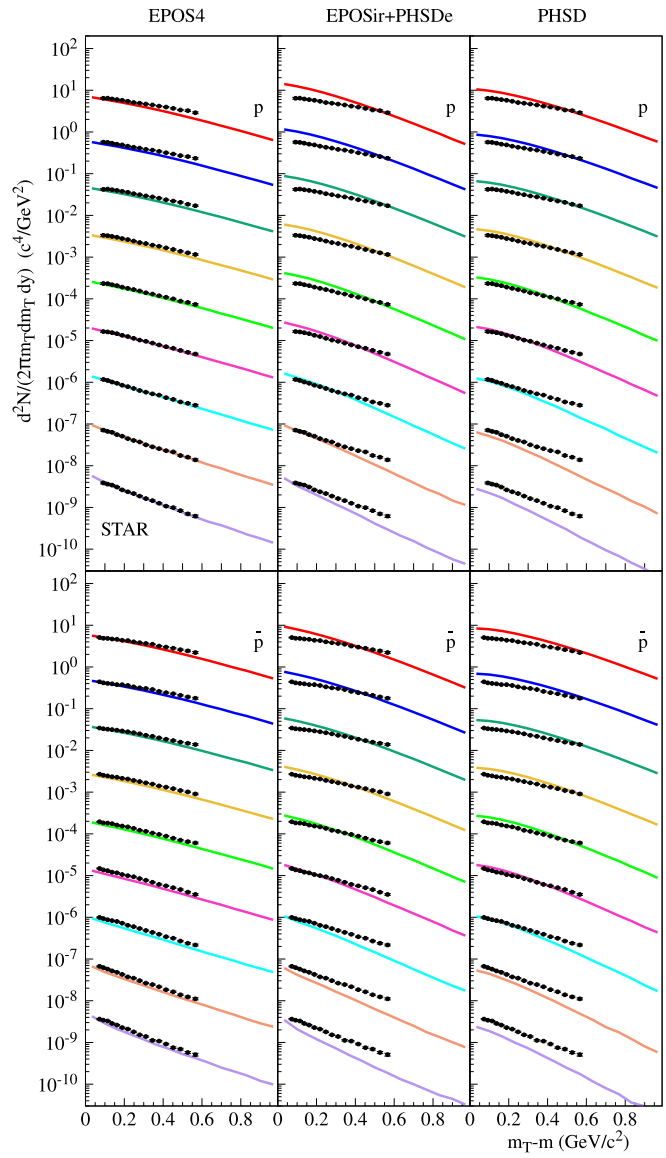


FIG. 15. Invariant yield as a function of transverse mass for p and $\bar{p}$ in Au + Au collision at $\sqrt{s_{NN}} = 200$ GeV at midrapidity ($|y| < 0.5$) for EPOS (left panel), EPOSir + PHSDe (middle panel) and PHSD (right panel). The m_T spectra are plotted for different centrality bins, from top to bottom: 0–5%, 5–10%, 10–20%, 20–30%, 30–40%, 40–50%, 50–60%, 60–70%, 70–80%, in each plot. The results are compared to the STAR experimental data [59] (black dots). All curves and experimental data are scaled by 10^{-n} starting from the top curve with 10^0.

C. Transverse momentum spectra

In this section, in Figs. 16–21, we present the invariant yields of identified hadrons as a function of transverse momentum p_T and centrality classes for the three models in comparison to experimental data for Au + Au collisions at top RHIC energy. Since the experimental p_T spectra are available up to large p_T values, it extends the comparison of transverse mass distributions from the previous section to a larger momentum space.

In Figs. 16, 17, and 18, we show the rapidity dependence of p_T spectra for pions $\pi^{\pm}$, kaons $K^{\pm}$, protons (p), and antiprotons ($\bar{p}$), for central (0–5%) Au + Au collisions at $\sqrt{s_{NN}} = 200$ GeV for EPOS (left panels), EPOSir + PHSDe (middle panels) and PHSD (right panels), in comparison to the BRAHMS experiment [57,58]. We note that the p and $\bar{p}$ spectra are shown with and without accounting for the weak decays since the experimental procedures consider weak decay products "partly." One can see that the pion and kaon spectra are well described by EPOS for all rapidity bins while

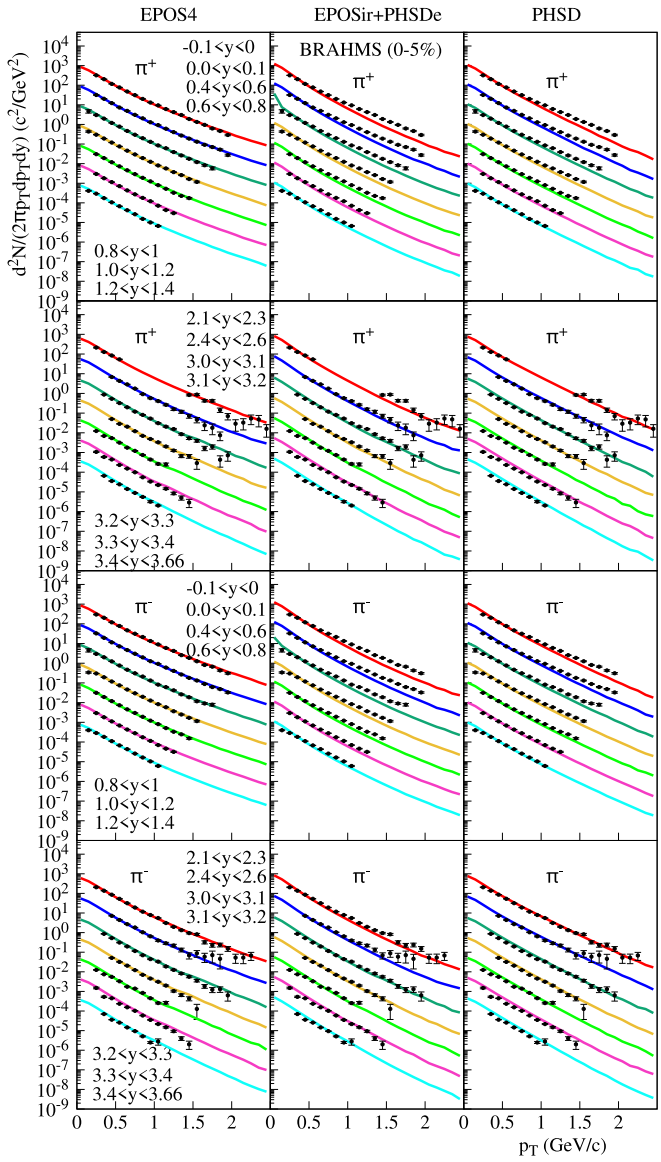


FIG. 16. Transverse momentum spectra of π^+ and π^- for selected rapidity intervals (from top to bottom $[-0.1, 0]$ to [3.4, 3.66]) for central (0–5%) Au + Au collisions at $\sqrt{s_{NN}} = 200$ GeV for EPOS (left panel), EPOSir + PHSDe (middle panel) and PHSD (right panel). No feed down from weak decays is accounted for. The experimental data are from the BRAHMS collaboration (black dots) [57]. Model results are scaled by 10^{-n}, starting from the top curve with 10^0.

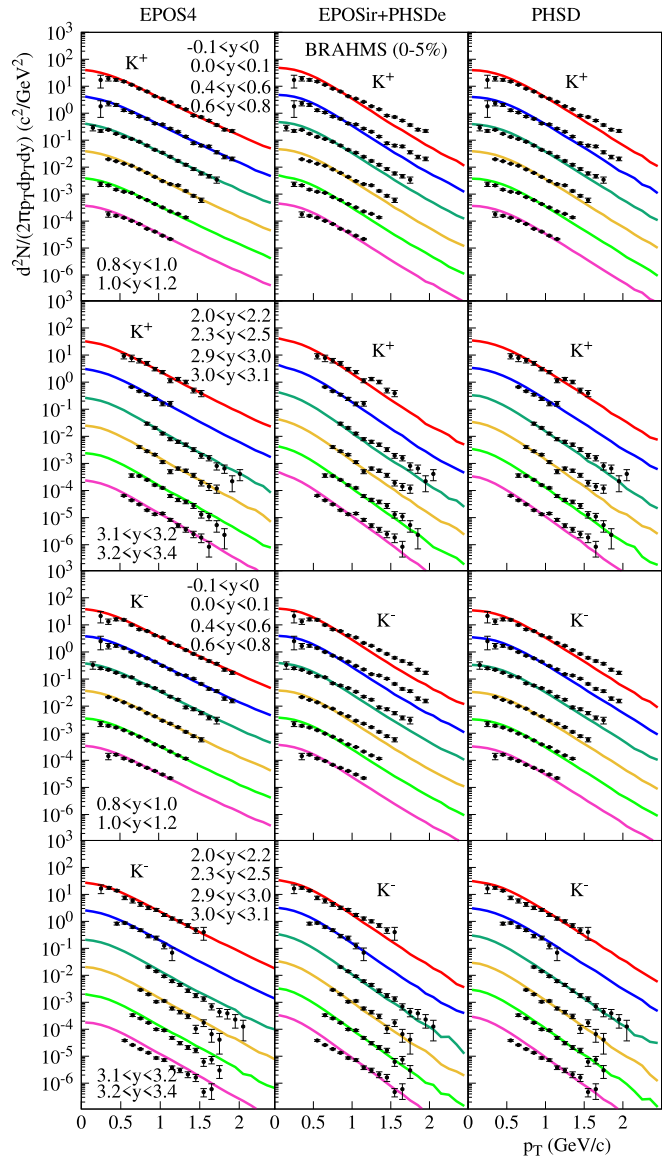


FIG. 17. Transverse momentum spectra of K^+ and K^- for selected rapidity intervals (from top to bottom $[-0.1, 0]$ to [3.2, 3.4]) for central (0–5%) Au + Au collisions at $\sqrt{s_{NN}} = 200$ GeV for EPOS (left panel), EPOSir + PHSDe (middle panel) and PHSD (right panel). Here, feed down from weak decays is accounted for. The experimental data are from the BRAHMS collaboration (black dots) [57]. Model results are scaled by 10^{-n}, starting from the top curve with 10^0.

the p_T spectra from PHSD and EPOSir + PHSDe are slightly softer for midrapidity bins. A similar trend is observed for the p, $\bar{p}$ spectra: the slope from EPOS is harder than from PHSD and EPOSir + PHSDe and better in line with the BRAHMS data.

Now we study the centrality dependence of the p_T spectra measured close to midrapidity for identified hadrons in Au + Au collisions at $\sqrt{s_{NN}} = 200$ GeV. We start with Fig. 19, which shows the invariant yields for charged hadrons as a function of p_T for 6 centrality bins (from top to bottom: 0–6%, 6–15%, 15–25%, 25–35%, 35–45%, and 45–50%), in a rapidity range of $0.2 < y < 1.4$, for EPOS (upper panel), EPOSir + PHSDe (middle panel), and PHSD (lower panel). The model results are compared to the experimental data from the PHOBOS collaboration (black dots) [60]. One can see that all models reproduce the low part of the spectra very well, however, the large p_T spectra are nicely reproduced only by EPOS while the PHSD and EPOSir + PHSDe underestimate the high p_T data.

A similar trend is obtained for the p_T spectra of identified hadrons, shown in Figs. 20 and 21. In particular, Fig. 20 shows the comparison of model calculations for p_T spectra

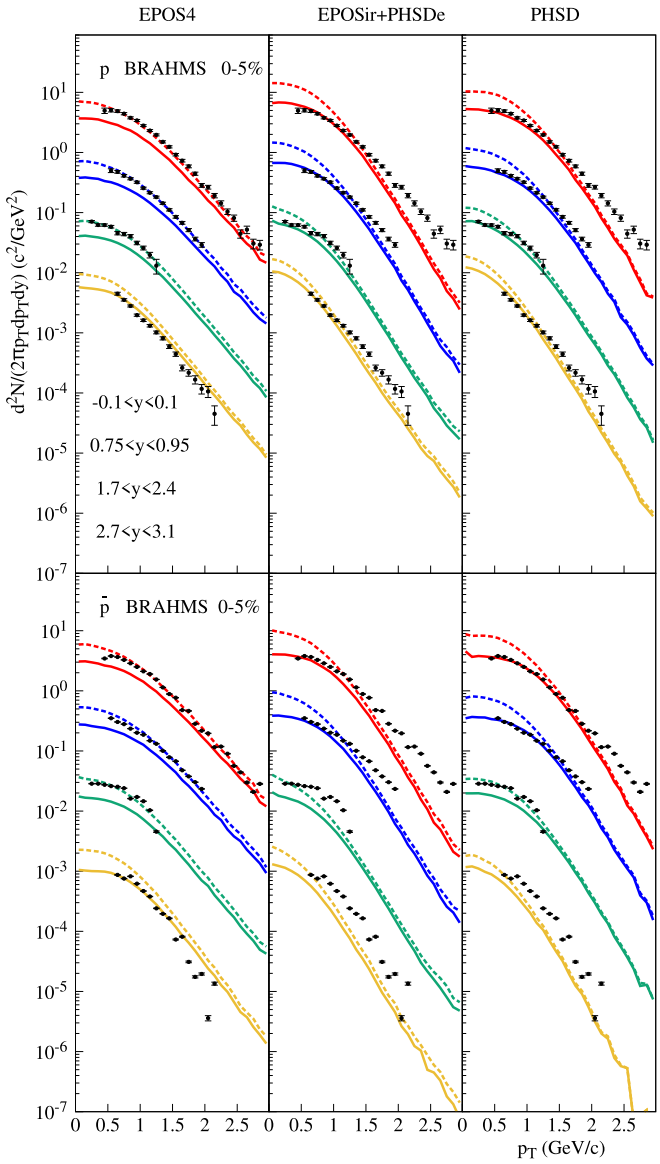


FIG. 18. Proton (p) and antiproton ($\bar{p}$) transverse momentum spectra for selected rapidity intervals (from top to bottom $[-0.1, 0.1]$ to $[2.7, 3.1]$) for central (0–5%) Au + Au collisions at $\sqrt{s_{NN}} = 200$ GeV for EPOS (left panel), EPOSir + PHSDe (middle panel) and PHSD (right panel). The dashed and solid lines show the results with and without accounting for weak decays, respectively. The experimental data are from the BRAHMS collaboration (black dots) [58] and model results are scaled by 10^{-n} and $(1/dy) \times 10^{-n}$, respectively, starting from the top curve with 10^0.

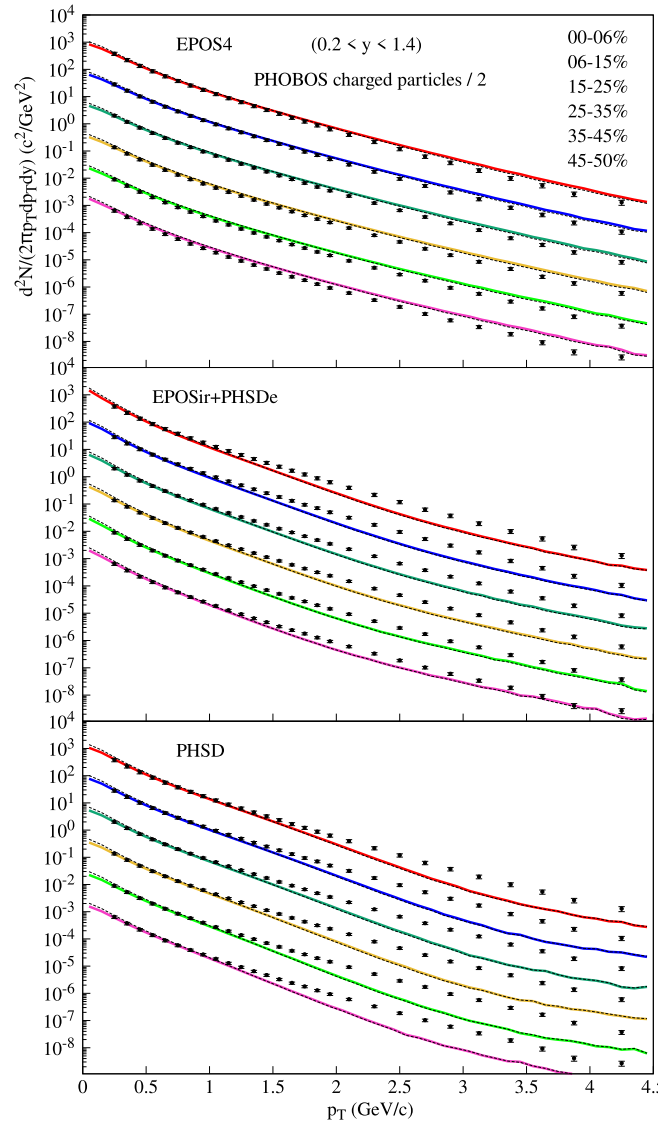


FIG. 19. Invariant yields for charged hadrons as a function of p_T for six centrality bins (from top to bottom: 0–6%, 6–15%, 15–25%, 25–35%, 35–45%, and 45–50%) in a rapidity range of $0.2 < y < 1.4$ for Au + Au collisions at $\sqrt{s_{NN}} = 200$ GeV for EPOS (upper panel), EPOSir + PHSDe (middle panel), and PHSD (lower panel). The experimental data from the PHOBOS collaboration (black dots) [60]. Simulation's results are scaled by 10^{-n} and $(1/dy) \times 10^{-n}$, respectively, starting from the top curve with 10^0. The dashed and solid lines show the results with and without accounting for weak decays, respectively.

of $\pi^{\pm}$, $K^{\pm}$, p, and $\bar{p}$ at midrapidity ($|y| < 0.5$) from most central (0–10%) to most peripheral (60–92%) collisions, versus STAR data [62]. Figure 21 presents the p_T spectra of K^0_S and strange (anti)baryons Λ, $\bar{\Lambda}$, Ξ^-, $\bar{\Xi}^+$, and $\Omega^- + \bar{\Omega}^+$, at midrapidity, from most central (0–5%) to peripheral collisions (60–80%). One can see the very good reproduction of all spectra by EPOS and the growing deviation from the experimental data with increasing p_T for PHSD and EPOSir + PHSDe.

We will discuss and interpret all these results later, but before doing so, we will have a closer look so some key elements of EPOS4, namely, the core-corona procedure and the choice of the shear viscosity.

D. Role of core-corona and viscosity in EPOS4

As explained in detail earlier, in EPOS4, primary interactions lead to the production of prehadrons and a core-corona procedure allows to separate the core and corona prehadrons.

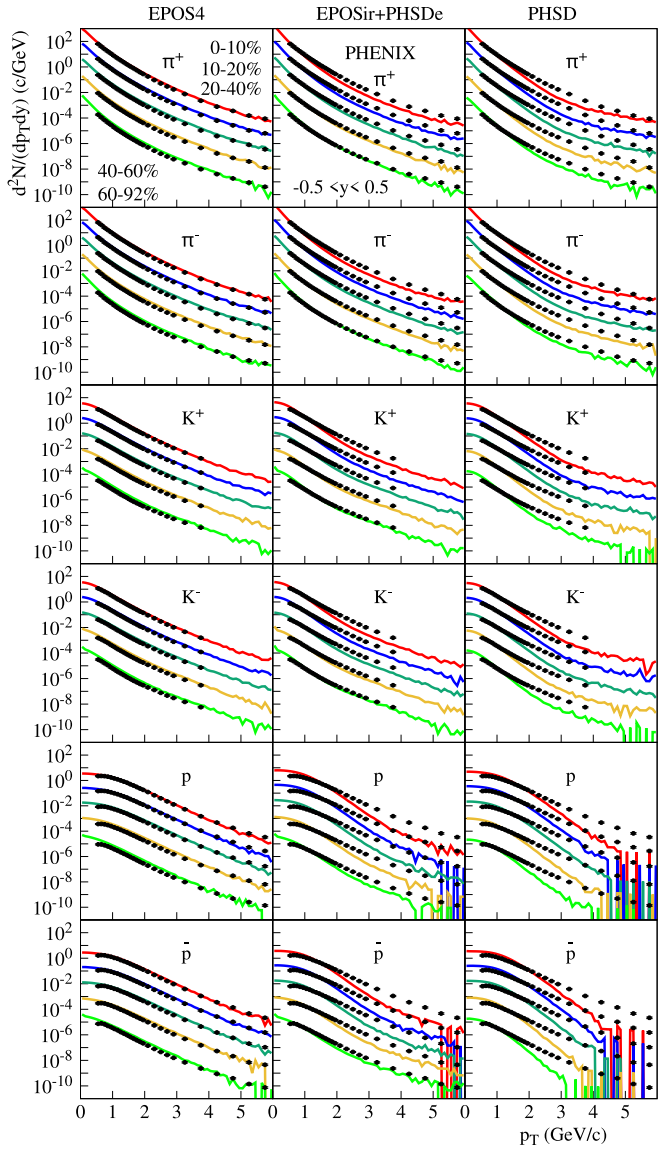


FIG. 20. Invariant yield of π^+, π^-, K^+, K^-, p, and $\bar{p}$ as a function of transverse momentum p_T at midrapidity ($|y| < 0.5$) for Au + Au collisions at $\sqrt{s_{NN}} = 200$ GeV, from central (0–10%) to peripheral (60–92%) collisions (from top to bottom in each plot), for EPOS (left panel), EPOSir + PHSDe (middle panel) and PHSD (right panel). The experimental data are taken from the PHENIX collaboration (black symbols) [61]. All curves and experimental data are scaled by 10^{-n} starting from the top curve with 10^0.

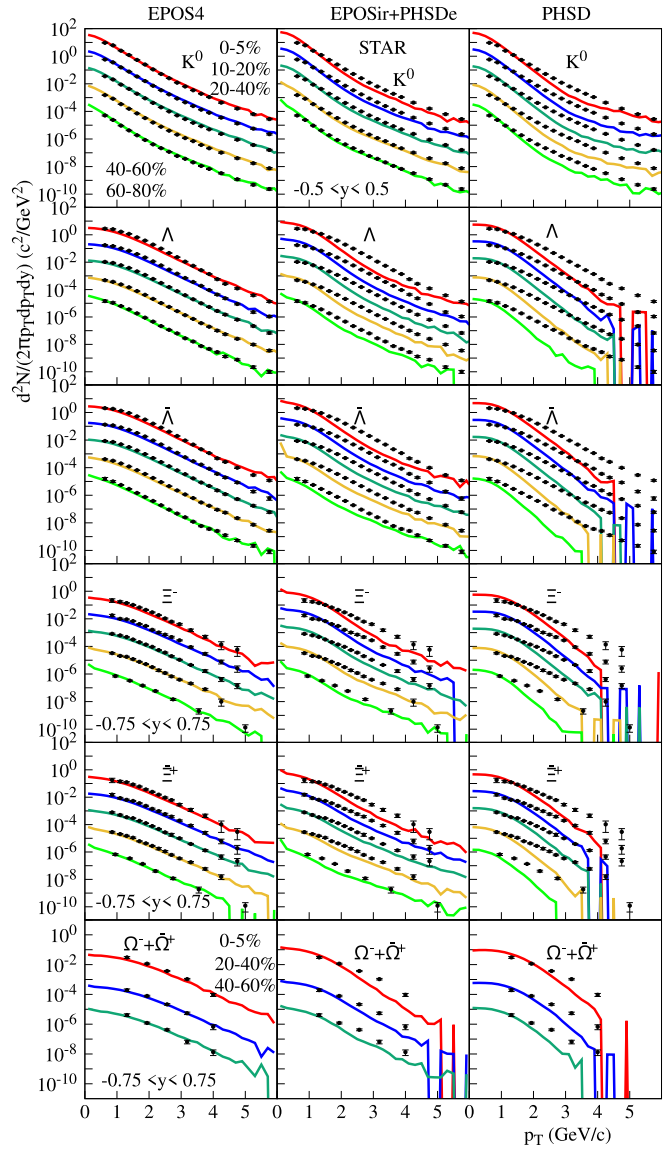


FIG. 21. Invariant yield of K^0_S, Λ, $\bar{\Lambda}$, Ξ^-, $\bar{\Xi}^+$, and $\Omega^- + \bar{\Omega}^+$ as a function of transverse momentum p_T at midrapidity for Au + Au collisions at $\sqrt{s_{NN}} = 200$ GeV from central (0–5%) to peripheral collisions (60–80%) (from top to bottom in each plot) for EPOS (left panel), EPOSir + PHSDe (middle panel), and PHSD (right panel). The experimental data are taken from the STAR collaboration (black dots) [62]. The experimental data and simulation's results are scaled by 10^{-n} and $(1/dy) * 10^{-n}$, respectively, starting from the top curve with 10^0.

The former constitute the core, the latter are considered to be hadrons. The core is meant to be matter, which evolves according to viscous hydrodynamics. After the hadronization of the fluid, the created hadrons as well as the corona prehadrons (having been promoted to hadrons) may still interact via hadronic scatterings.

The core-corona procedure was first introduced in Ref. [17] and updated in Ref. [19]. The current implementation is discussed in detail in Ref. [14].

In the following, in Figs. 22 and 23, we show separately core and corona contributions to hadron production in EPOS4, to better understand the results. We distinguish:

(A) The "core+corona" contribution: primary interactions (*S*-matrix approach for parallel scatterings), plus core-corona separation, hydrodynamic evolution, and microcanonical hadronization, but without hadronic rescattering.
(B) The "core" contribution: as case (A), but considering only core particles.
(C) The "corona" contribution: as case (A), but considering only corona particles.
(D) The "full" EPOS4 scheme: as case (A), but in addition hadronic rescattering.

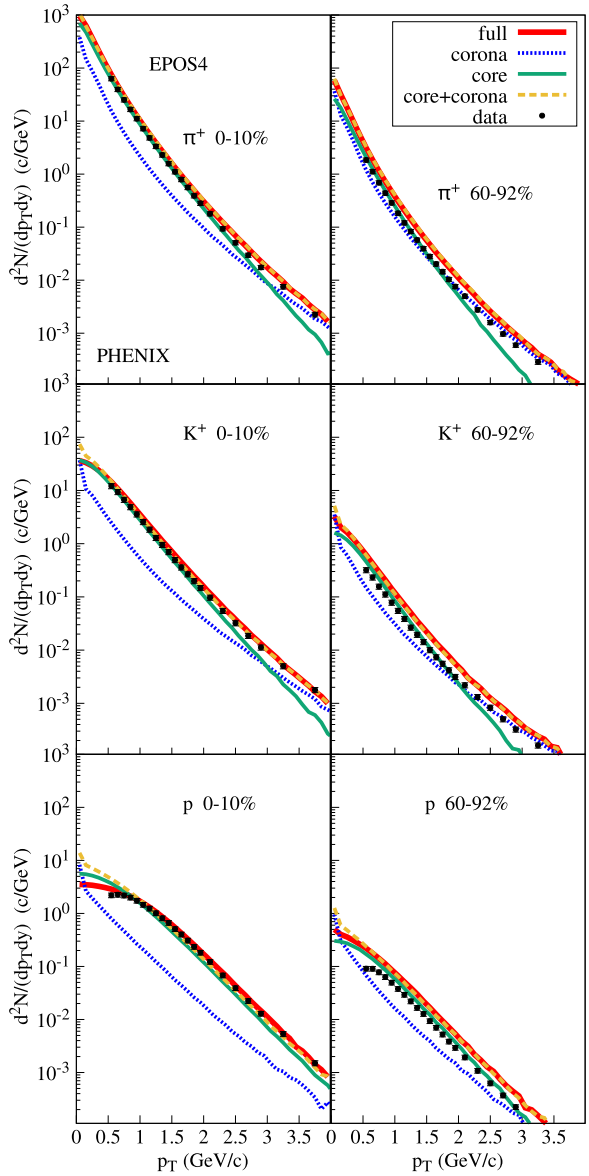


FIG. 22. Invariant yield of π^+, K^+, and p, as a function of transverse momentum p_T, at midrapidity ($|y| < 0.5$) for Au + Au collisions at $\sqrt{s_{NN}} = 200$ GeV for most central (0–10%), and peripheral (60–92%) collisions, for EPOS simulations. The thick red, dotted blue, green, and dashed yellow lines indicate the full (EPOS + hydro +UrQMD), corona, core, and core + corona results. The experimental data are taken from the PHENIX collaboration (black symbols) [61].

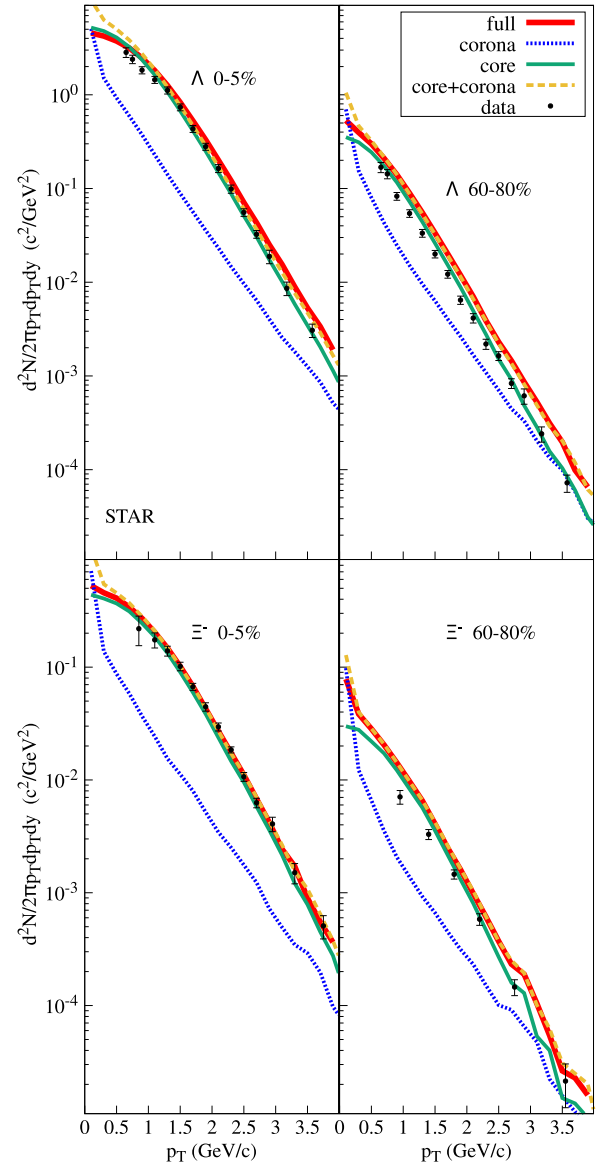


FIG. 23. Invariant yield of Λ and Ξ^-, as a function of transverse momentum p_T, at midrapidity for Au + Au collisions at $\sqrt{s_{NN}} = 200$ GeV for most central (0–5%), and peripheral (60–80%) collisions, for EPOS4 simulations. The thick red, dotted blue, green, and dashed yellow lines indicate the full (EPOS+hydro +UrQMD), corona, core, and core+corona results. The experimental data are taken from the STAR collaboration (black dots) [62].

In cases (A), (B), and (C), we need to exclude the hadronic afterburner, because the latter affects both core and corona particles, so in the full approach, the core and corona contributions are not visible anymore.

In Fig. 22, the invariant yield of π^+, K^+, and p, is shown as a function of transverse momentum p_T, at midrapidity ($|y| < 0.5$) for Au + Au collisions at $\sqrt{s_{NN}} = 200$ GeV for most central (0–10%), and peripheral (60–92%) collisions, for EPOS simulations. The experimental data are taken from the PHENIX collaboration (black symbols) [61]. We show separately the different contributions, as discussed in the following.

The green curves refer to the core contribution, i.e., particles produced from the hadronization of the fluid. Most importantly, the latter carry the collective motion (flow velocity) of the fluid, which can be clearly seen at intermediate values of p_T (1–4 GeV/c). Comparing the green core curves for pions, kaons, and protons, one can see that the form changes dramatically: if goes from convex (for pions) to concave (for protons). The important property is the mass of the particles. Since flow is given in terms of velocity, the effect

on the transverse momentum is bigger for heavy compared to light particles, because we have "momentum = mass times velocity." So we get a very strong flow effect for protons, compared to pions. Although pions are much more frequent than protons, the yields are comparable at p_T values of 3–4 GeV/c.

The dotted blue curves refer to the corona contribution, i.e., particles which did not take part in the collective hydrodynamic evolution, but having been produced directly from string decays. If one would multiply the kaon curve by two and the proton one by four, then the three curves are very close, apart of a bigger yield for pions at small p_T (resonance production). So at intermediate values of p_T, it is clearly the flow, visible in the core contribution, which makes a difference between light and heavy particles.

The dashed yellow curves indicate core+corona results, i.e., the sum of the core and the corona curves. All this (core-corona / core+corona) refers to simulations without hadronic rescattering. Including the latter, on gets the "full" results, shown as thick red lines (the final result). There is a sizable effect (difference between red and yellow) for protons, but anyway small compared to the flow effect. Comparing the left and the right column in Fig. 22, we see that the core effect is much smaller in peripheral collisions (as expected).

In Fig. 23, we show the different contributions for hyperons, which confirms the above discussion, saying that there is a core effect (increased yields at intermediate values of p_T due to flow), which increases with particle mass. Finally, we note that the "crossing point" of the green and dotted blue curves (from where on the "hard" corona dominates) is at around 3 GeV/c for pions in central collisions, but gets to much larger values with increasing particle mass.

In Figs. 24 and 25, we investigate another important issue, namely, the dependence of EPOS4 results on the shear viscosity. In Fig. 24, we show p_T spectra for different particle species for Au + Au collisions at $\sqrt{s_{NN}} = 200$ GeV, for central and peripheral collisions. We show EPOS4 results, using the standard value of o η/s of 0.08 (solid red lines) and compare it to results obtained for η/s of 0.24 (dashed blue lines). The latter are a little bit harder, but the difference is small. Figure 25 shows, that the pseudorapidity distributions get a little bit higher, for $\eta/s = 0.24$ compared to 0.08.

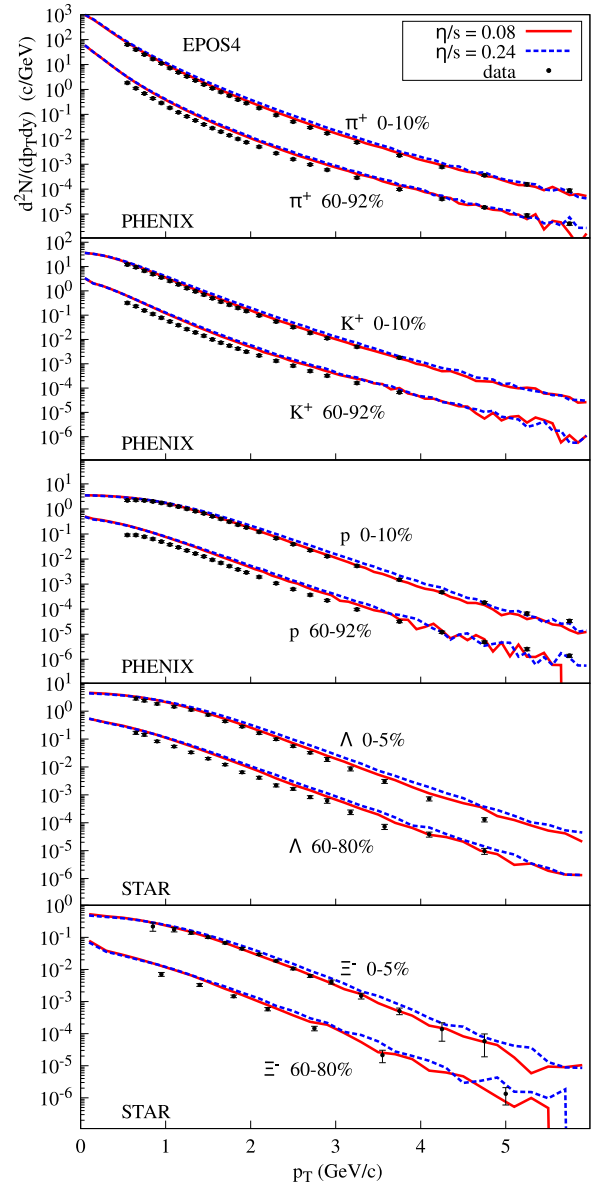


FIG. 24. Invariant yield of π^+, K^+, p, Λ, and Ξ^-, as a function of transverse momentum p_T, at midrapidity, for Au + Au collisions at $\sqrt{s_{NN}} = 200$ GeV, for central and peripheral collisions, for EPOS simulations. The solid red curves refer to η/s of 0.08, the dashed blue ones to 0.24. The experimental data (black dots) are taken from the PHENIX collaboration [61] and from the STAR collaboration [62].

E. Messages from the spectra comparison

The obtained results for the transverse momentum spectra can be interpreted as follows: (1) the fact that EPOS and EPOSir + PHSDe, which start with identical initial conditions, but follow a different dynamical evolution, end up with different transverse spectra, as well as (2) the fact that EPOSir + PHSDe and PHSD, which start with completely different initial conditions, but follow approximately a similar dynamical evolution, end up with rather similar spectra, indicate the dominant role of the dynamical evolution versus the initial conditions for the bulk observables such as transverse momentum/mass spectra. The transverse momentum spectra at intermediate values of p_T (1–5 GeV/c) are especially sensitive to this balance, i.e.,

(1) EPOS starts with strongly fluctuating initial conditions in space, transforming quickly into large (compared to PHSD) flow (and anisotropic flow, cf. Fig. 10). This is due to EPOS' core-corona separation, converting the core part into a hydrodynamically evolving matter, assuming very early local thermalization. The hydrodynamics in EPOS produces at very early times a very strong radial flow, which leads to an enhancement of particle production at intermediate values of p_T, in particular for heavy particles, as discussed in the preceding section.

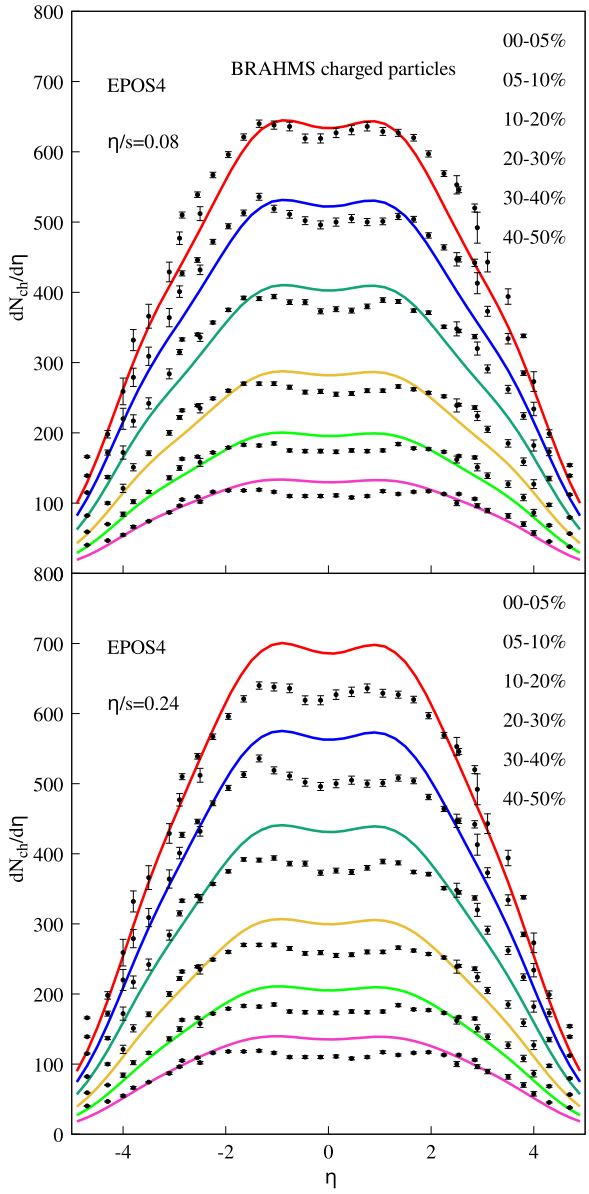


FIG. 25. Charged particle distribution ($dN_{\rm ch}/d\eta$), as a function of pseudorapidity (η), for Au + Au collisions at $\sqrt{s_{NN}} = 200$ GeV, for EPOS simulations, from central to semiperipheral collisions (from top to bottom: 0–5%, 5–10%, 10–20%, 20–30%, 30–40%, and 40–50%). The upper panel refers to η/s of 0.08, the lower to 0.24. The experimental data (black dots) are taken from the BRAHMS collaboration [30].

(2) In PHSD, the initial conditions, build by primary high-energy NN interactions—realized via the LUND string model—are less fluctuating than in EPOS since in PHSD the interactions are treated in a probabilistic manner as independent sequences of collisions in time defined by Monte Carlo according to the total NN cross-sections. Contrarily, in EPOS the initial collisions are considered as instantaneous multiple scatterings, modeled in terms of a summation of amplitudes within S-matrix theory, which allows to account for the interferences of amplitudes. The treatment of the QGP in the PHSD provides a good description of the "thermal part" (low p_T) of the spectra, but leads to softer spectra at intermediate values of p_T compared to EPOS as well as to the data. The latter can be attributed partially to the modeling of hadronization in PHSD which favors the combination of low p_T partons according to the covariant transition rate [20].

(3) EPOSir + PHSDe is based on the EPOS initial conditions, but follows the PHSD dynamical evolutions. There is no assumption of equilibration. Contrary to the hydrodynamic evolution, the PHSD evolution does not transform the intial space fluctuatins (with local high density "hot spots") into large flow, and leads to results which are much closer to PHSD than to EPOS proving the dominant influence of the dynamics. This finding is in line with an early PHSD study which shows that the size of the initial fluctuations doesn't influence much the final spectra and harmonic flow results [63]. The latter we will check in the next section.

V. ANISOTROPIC FLOW

The study of the azimuthal distribution of particle production provides important information about the system's space-time evolution. The anisotropies in the initial geometry of the collisions may be transformed via pressure gradients to the anisotropies in the final state momentum distribution, the latter being accessible experimentally. The discovery of a large azimuthal anisotropic flow of hadrons at RHIC [64] provided one of the first strong signals for dense partonic matter formation in ultrarelativistic nucleus-nucleus collisions, producing hydrodynamic flow, investigated also in EPOS [18] and PHSD [24].

A. Results for flow harmonics

The event plane (EP) approach [67,68] has been used in the RHIC experiments we are going to compare with, and in our analysis. One uses the Fourier series, i.e.,

$$\frac{d^3N}{d^2p_T d\eta} \propto \left\{1 + 2\sum_{n=1}^{\infty} v_n(p_T,\eta)\cos[n(\phi - \Psi_{\rm EP})]\right\}, \quad (8)$$

where p_T is the transverse momentum of a particle, ϕ the azimuthal angle, η the pseudorapidity, and $\Psi_{\rm EP}$ the event plane angle. Elliptic flow is represented by $v_2 = \langle\cos[n(\phi - \Psi_{\rm EP})]\rangle$, where the angular brackets denote an average over the particles and events.

In Figs. 26 and 27, we present the results for the flow harmonics v_2 of the three models, EPOS (dashed blue curves), EPOSir + PHSDe (solid red curves), and PHSD (dotted green curves), and compare them to experimental data. In Fig. 26, we show the differential flow $v_2(p_T)$ of π, K, and p using the EP method for Au + Au at $\sqrt{s_{NN}} = 200$ GeV for different centralities for EPOS, EPOSir + PHSDe, and PHSD. In our analysis, we applied the cut $|\eta| < 0.35$ as in the PHENIX experiment [65]. EPOS provides a good description of elliptic flow v_2 for π, K, and p for the whole p_T range. PHSD describes reasonably well the proton v_2 for all centralities as well as for kaons up to 2 GeV/c, while the pions v_2 deviate

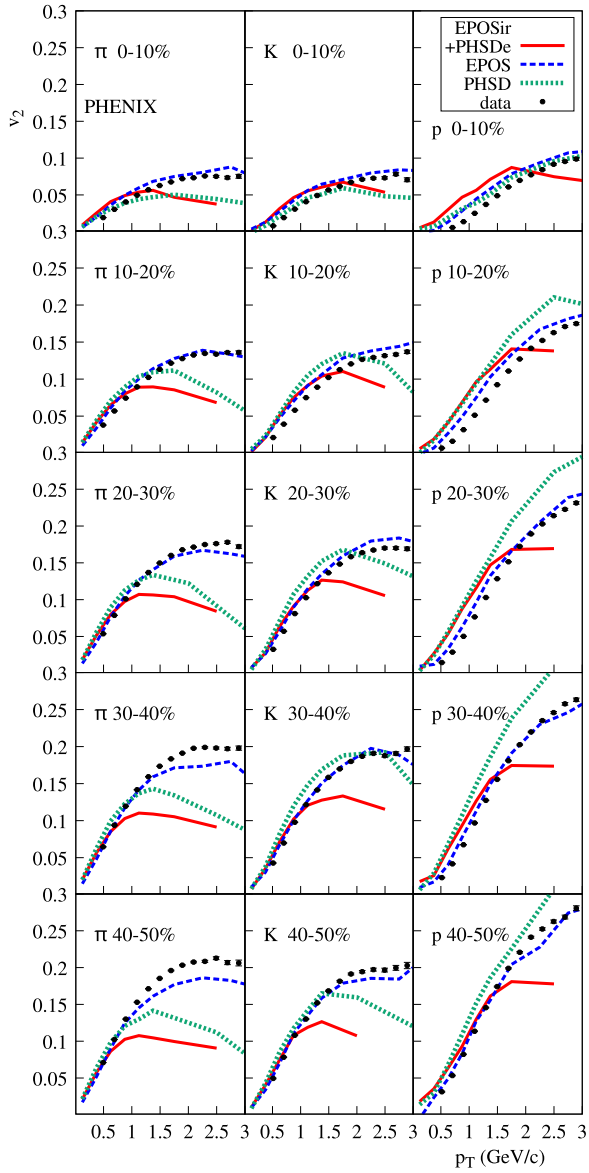


FIG. 26. Differential elliptic flow (v_2) of π, K, and p, as a function of transverse momentum p_T, at midrapidity, for Au + Au collisions at $\sqrt{s_{NN}} = 200$ GeV, for different centrality bins. Dashed blue, solid red, and dotted green lines indicate the EPOS, EPOSir + PHSDe and PHSD results, while the black dots show the PHENIX experimental data [65], respectively.

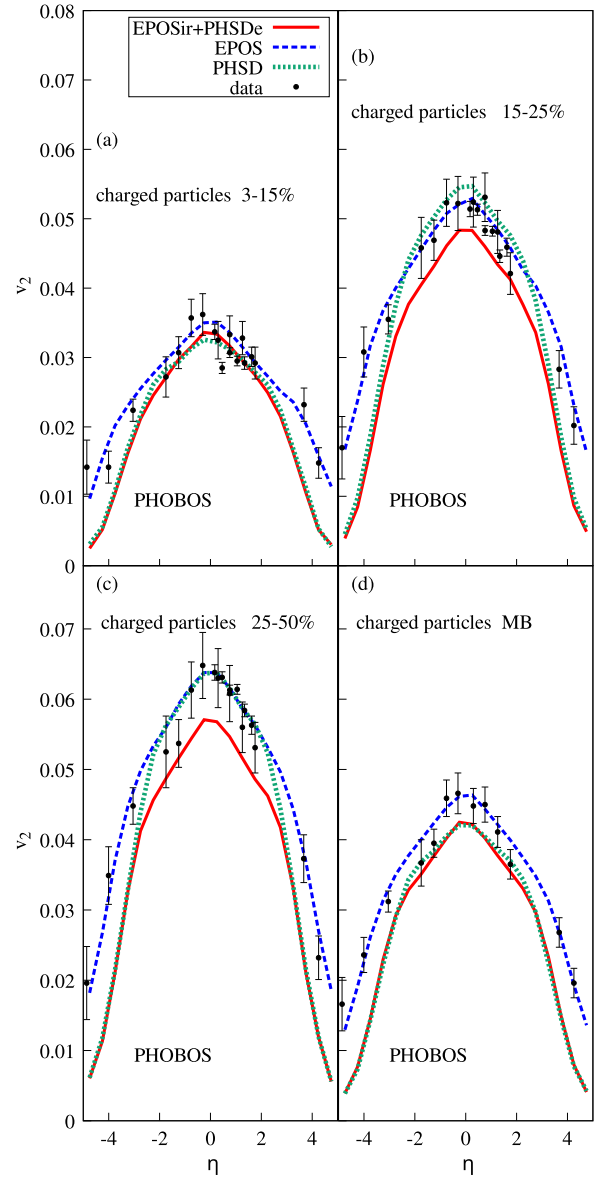


FIG. 27. Elliptic flow as a function of pseudorapidity [$v_2(\eta)$] for charged hadrons in Au + Au collisions at $\sqrt{s_{NN}} = 200$ GeV, for different centrality classes, i.e., (a) 3–15%, (b) 15–25%, (c) 25–50%, and (d) minimum bias (MB). Dashed blue, solid red, and dotted green lines indicate the EPOS, EPOSir + PHSDe, and PHSD results, while the black dots show the PHOBOS experimental data [66], respectively.

from the data already at $p_T > 1$ GeV/c. The elliptic flow from EPOSir + PHSDe is closer to the PHSD results and even slightly lower for pions and kaons and high momentum protons. The lowering of the v_2 in EPOSir + PHSDe relative to the PHSD is in line with the time evolution of momentum eccentricity ϵ_P in Fig. 10, which shows that ϵ_P of EPOSir + PHSDe develops slower than the PHSD one and ends with slightly lower averaged value. For both, EPOSir + PHSDe and PHSD, ϵ_P grow much less with time than the EPOS curve.

In Fig. 27, we show the elliptic flow $v_2(\eta)$ as a function of pseudorapidity for charged hadrons from central to semiperipheral as well as for minimum bias Au + Au collisions at $\sqrt{s_{NN}} = 200$ GeV for the three models in comparison to the experimental data from the PHOBOS collaboration [66]. The v_2 from all models and data decreases toward central collisions. As follows from the figure, PHSD provides a good description of the experimental data at midpresudorapidity, in spite the fact that PHSD underestimates $v_2(p_T)$ for large p_T. That is due to the high abundance of hadrons with low p_T which dominantly contribute to $v_2(\eta)$ integrated over all p_T. EPOS provides as well a good description of the data. The EPOSir + PHSDe flow is slightly lower. The $v_2(\eta)$ distribution from EPOS is much wider than those from other two

models and has a non-Gaussian shape. Thus, $v_2(\eta)$ indicates how the pressure is redistributed over rapidity in the system.

Before discussing and interpreting these results, we will again first discuss some issues related to EPOS4.

B. Role of core-corona and viscosity in EPOS4

As already discussed earlier, the core-corona procedure is a crucial element in the EPOS picture, in particular the role of the core, expanding as a fluid, developing a strong flow. This has a very strong effect on spectra, as already discussed, but also on the v_n distributions. We will discuss in the following the individuel contributions of core and corona for v_2 and show results in Fig. 28. The other element to be discussed is the dependence of results on the shear viscosity, which will be studied as well in Figs. 29 and 30.

Concerning the core-corona contributions, we will distinguish again (A) the "core+corona" contribution, being the full simulation (parallel scatterings, core-corona separation, hydrodynamic evolution, and microcanonical hadronization) but without hadronic rescattering; (B) the "core" contribution being the same as (A), but considering only core particles; (C) the "corona" contribution, being the same as (A), but considering only corona particles; (D) the "full" EPOS4 scheme, namely, as (A), but in addition hadronic rescattering. In Fig. 28, we show differential elliptic flow (v_2) of π, K, p, and charged particles, as a function of transverse momentum p_T, at midrapidity, for Au + Au collisions at $\sqrt{s_{NN}} = 200$ GeV, for central (0–5%) and midperipheral (40–50%) collisions, for EPOS simulations. Thick red, dotted blue, green, and dashed yellow colors indicate the full (EPOS+hydro+UrQMD), corona, core, and core+corona results, while the black dots show the PHENIX experimental data [65], respectively.

Naively one would expect zero elliptical flow for the corona part (dotted blue curves). This is actually what we get doing a simulation without hydro, where particle production comes from string decay, being perfectly symmetric. Here, the values obtained from the simulation are very small, but not exactly zero. This is due to the fact that the core-corona procedure itself may introduce an azimuthal asymmetry. But the effect is small.

Looking at the v_2 curve for the core (green curve), it increases continuously, overshooting finally the data. This is in particular visible for the intermediate centralities (40–50%) where the v_2 values are largest.

Now let us look at the dashed yellow curves, the core+corona contribution. We have seen that corona alone gives a very small v_2 result, therefore when considering both, particles from corona and core, the former bring the v_2 of the core particles down. So the dashed yellow curves are somewhat below the green ones. Interesting is the fact that the yellow core+corona curves even bend down at high p_T, similar as the data. This "bending down" is a typical core-corona effect in the EPOS framework.

Finally, we come to the thick red "full" curve, representing the final result, based on all particles. The difference between the yellow core+corona curve and the red one is the fact that the hadronic cascade is considered in the latter. So the

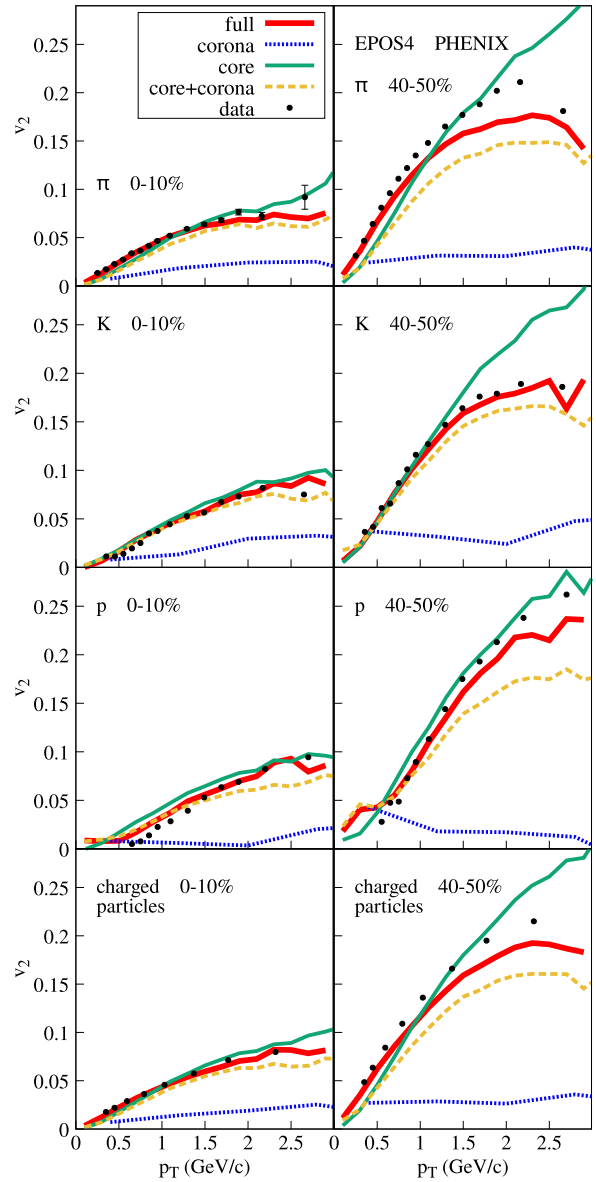


FIG. 28. Differential elliptic flow (v_2) of π, K, p, and charged particles, as a function of transverse momentum p_T, at midrapidity, for Au + Au collisions at $\sqrt{s_{NN}} = 200$ GeV, for central (0–5%) and midperipheral (40–50%) collisions, for EPOS simulations. Thick red, dotted blue, green, and dashed yellow lines indicate the full (EPOS+hydro + UrQMD), corona, core, and core + corona results, while the black dots show the PHENIX experimental data [65], respectively.

effect of the hadronic cascade is to increase v_2, more or less pronounced depending on the particle species.

So we see that also the v_2 curves (and more generally v_n) are strongly affected by the core-corona mechanism.

In Figs. 29 and 30, we consider the p_T and the η distributions of v_2, compared to data, already seen earlier. But here we compare simulations for η/s of 0.08 (solid red curves) and those for η/s of 0.24 (dashed blue curves). The difference is small. It should be said that EPOS employs "a rapid hadronization" according to microcanonic decay, and not a

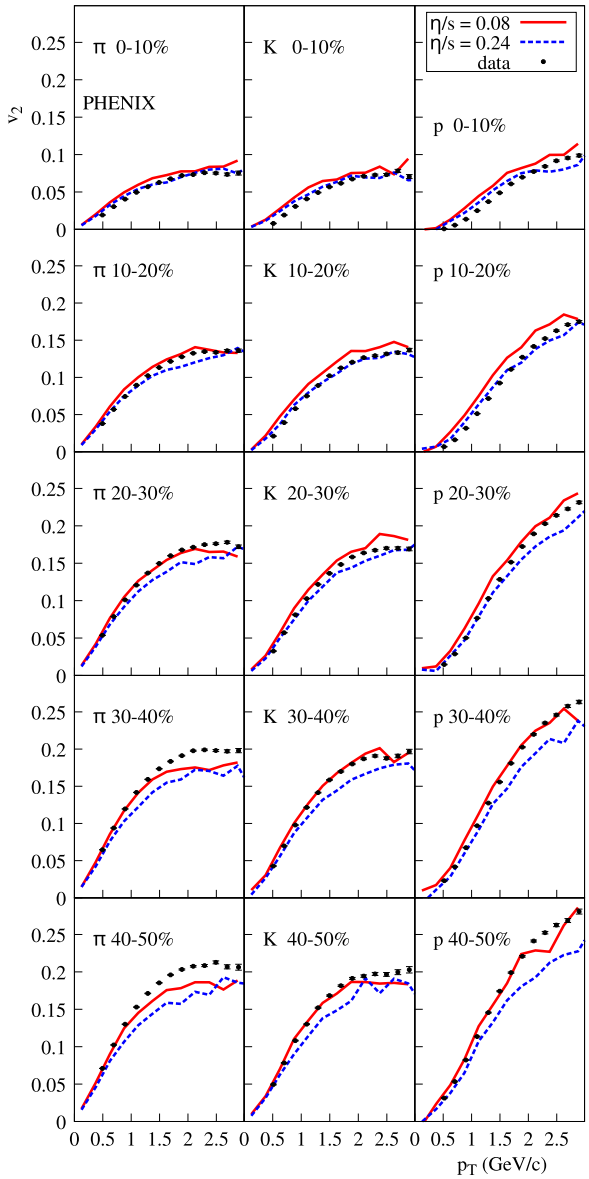


FIG. 29. Differential elliptic flow (v_2) of π, K, and p, as a function of transverse momentum p_T, at midrapidity, for Au + Au collisions at $\sqrt{s_{NN}} = 200$ GeV, for different centrality bins. The solid red curves refer to η/s of 0.08, the blue dashed ones to 0.24. The black dots show the PHENIX experimental data [65].

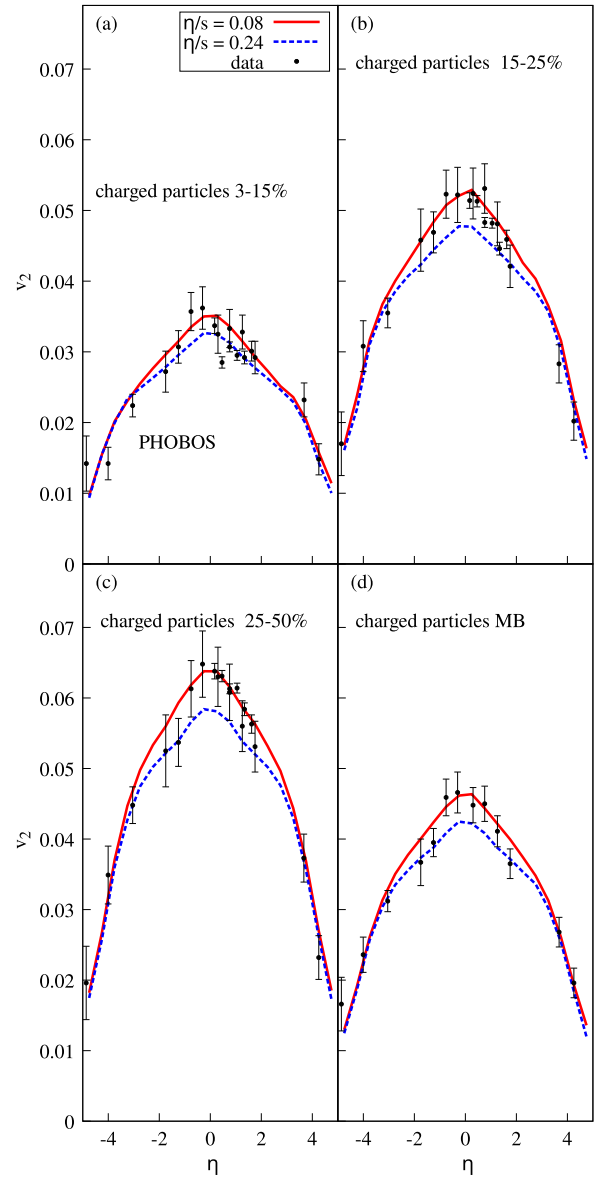


FIG. 30. Elliptic flow as a function of pseudorapidity [$v_2(\eta)$] for charged hadrons, in Au + Au collisions at $\sqrt{s_{NN}} = 200$ GeV, for different centrality classes, i.e., (a) 3–15%, (b) 15–25%, (c) 25–50%, and (d) minimum bias (MB). The solid red curves refer to η/s of 0.08, the dashed blue ones to 0.24. The black dots show the PHOBOS experimental data [66].

Cooper-Frye method with "viscous corrections." So in EPOS, the effect of viscosity is only due to the modification of the fluid dynamics, and not related to the hadronization.

The microcanonic decay is decribed in very much detail in Ref. [14]. It is one of the highlights of EPOS4, with newly developed powerful methods for the decay, but also concerning the four-momentum flow through the freezeout hypersurface. This allows to define the corresponding four-velocity, which is finally used to "give this flow back" to the produced hadrons (see section "Flow through hypersurface elements" of Ref. [14]).

C. Messages from the flow harmonics comparison

Considering the p_T dependence, we observe that EPOS provides the best description of v_2 for π, K, and p. We have seen that the hight p_T behavior in EPOS is strongly affected by the core, representing hydrodynamic flow. The final phase (hadronic cascade) also matters, but crucial is the flow of the core, which develops very early. EPOSir + PHSDe and PHSD deviate from data with increasing p_T. This is in line with the time evolution of momentum eccentricity ϵ_P in Fig. 10, where EPOS shows a stronger increase than EPOSir + PHSDe and PHSD. The fact that the flow harmonics $v_2(p_T)$ from EPOSir + PHSDe are closer to PHSD, not to

EPOS, supports our conclusions from the previous section that the dynamical evolution is more important than the initial conditions.

Concerning the pseudorapidity dependence, we note that the ability of PHSD to describe well the flow v_n data at midrapidity and at low $p_T \leqslant 1$ GeV/c has been reported in our early studies [23,24,52,63] and is related to the dominant role of the QGP at low p_T at midrapidity. Since the QGP dynamics is well kept in PHSD by the DQPM model which follows the lQCD EoS, the PHSD reproduces the quark number scaling [23] and provides a good description of the bulk and flow observables of final hadrons.

The high p_T part is more sensitive to the spatial fluctuations in the initial conditions and the consequential strong radial flow, based on the core-corona separation, which is absent in the PHSD and is the key conceptual idea of the EPOS model. As has been discussed already several times, this core-corona separation in connection with the use of hydrodynamics—which assumes a full early thermalization of the matter—leads to the successful transformation of initial spatial anisotropy to final state momentum asymmetry. This is not observed in EPOSir + PHSDe.

VI. SUMMARY

In this study, we have investigated the relative impact of initial conditions and the dynamical evolution on the final observables in relativistic heavy-ion collisions. To achieve this goal, we developed a novel EPOSir + PHSDe framework, which utilizes EPOS initial conditions (EPOSi), complemented by a rope mechanism (EPOSir), followed by the nonequilibrium evolution within the PHSD approach (PHSDe). For comparison, we consider three models:

(1) *EPOS* employs instantaneous (parallel) multiple scatterings in an *S*-matrix approach, followed by a core-corona separation, a hydrodynamic evolution of the quark-gluon plasma phase, and hadronic rescatterings using UrQMD.
(2) *PHSD* initiates with primary high-energy independent nucleon-nucleon scattering via the LUND string model and evolves in time using fully microscopic transport dynamics for both partonic and hadronic matter.
(3) EPOSir + PHSDe combines the EPOS initial conditions with the PHSD dynamical evolution.

By comparing EPOSir + PHSDe with EPOS, we analyze the impact of different evolution models while keeping the initial conditions identical. Conversely, by comparing EPOSir + PHSDe with PHSD, we isolate the effects of different initial conditions for the same evolution model. This approach allows us to disentangle the influence of initial conditions from that of the dynamical evolution.

For model validation, we focus on Au + Au collisions at an invariant energy of $\sqrt{s_{NN}} = 200$ GeV, where the QGP volume is substantial. We examine bulk matter observables and anisotropic flow to assess the role of initial conditions and the dynamical evolution in heavy-ion collisions. Our findings can be summarized as follows:

(1) We found that using EPOSi leads to a strong overestimation of the final hadron yield when employing PHSDe. This "overproduction" is needed when using hydro, since the latter will reduce particle production because a large part of the energy is converted into flow and into work. The introduction of the ropes, i.e., the method "EPOSi+ropes" (EPOSir in short), decreased the number of prehadrons. Thus, the ropes allow to convert the initial large mass production in the Pomeron picture in EPOS to kinetic energy degrees-of-freedom.
(2) By studying the radial expansions via momentum eccentricities ϵ_P, we find that the system in EPOSir + PHSDe and PHSD expands more slowly in transverse direction and ϵ_P reaches saturation compared to the EPOS momentum eccentricity, which grows monotonically in time. Moreover, the EPOS ϵ_P increases very strongly (with large fluctuations) at very early times. In EPOSir + PHSDe, ϵ_P even decreases right after the start time, showing much less fluctuations compared to EPOS. The average $\langle\epsilon_P\rangle$ saturates at approximately the same value as in PHSD. This highlights the dominant influence of the evolution dynamics over the initial conditions. The difference in modeling the evolution between EPOS and PHSD leads to distinct behaviors in ϵ_P. In EPOS, the monotonic increase in momentum eccentricities is driven by its hydrodynamic description of the QGP. Conversely, in PHSD the QGP dynamics is modeled using the lQCD EoS and described in terms of off-shell massive partons within the DQPM framework.
(3) By studying the transverse momentum/mass spectra as well as rapidity distributions of hadrons, we find that EPOS accurately reproduces data for the charged particle spectra at all p_T including intermediate and high p_T, while PHSD and EPOSir + PHSDe show more soft spectra, and in spite that both models describe well the low part of the p_T spectra, they deviate from the data at intermediate and high p_T.
(4) Similar observations hold for the p_T behavior of the flow harmonics $v_2(p_T)$: a very good description of v_2 for all p_T by EPOS and deviation from the data for EPOSir + PHSDe and PHSD with increasing p_T. However, PHSD provides a good description of the pseudorapidity distribution of $v_2(\eta)$ which is dominated by low momentum hadrons.

The observation that EPOS and EPOSir + PHSDe, despite starting from similar initial conditions but following different dynamical evolutions, yield different results for hadron spectra and flow harmonics $v_n(p_T)$, and that EPOSir + PHSDe and PHSD, which begin with entirely different initial conditions but follow a similar dynamical evolution, produce approximately the same hadron spectra and v_n, highlights the dominant influence of the dynamical evolution on these observables over the initial conditions. The dynamical evolution finally defines how the initial conditions are evolved in time.

We can highlight the most important aspects in modeling of the dynamical evolution in the interplay with the initial

conditions using the EPOS, PHSD and EPOSir + PHSDe as follows:

(1) The ability of EPOS for a very good description of the p_T-dependence of bulk and flow observables can be attributed to the modeling of the initial stage using instantaneous (parallel) multiple scatterings, with a strongly fluctuating space anisotropy, the separation of the produced particles into core and corona, where the former is converted to a hydrodynamical description (which assumes local equilibration) at an early time, which creates very quickly flow and large (strongly fluctuating) momentum anisotropies, where the hydrodynamic evolution also converts a large fraction of the initial system energy into kinetic energy of expanding matter.

(2) In PHSD the good description of low p_T and underestimation of the high and intermediate p_T hadron spectra and flow v_n can be related (in comparison to EPOS) to: building of the initial phase by independent sequences of high-energy NN scatterings (using the LUND string model) which leads to more smooth initial conditions than in EPOS, being a fully microscopic nonequilibrium model, PHSD propagates hadronic and partonic degrees of freedom explicitly. On one side it allows to avoid discontinuities (e.g., a jump in entropy and energy density) attributed to the transition from initial conditions to a hydrodynamical description as well as to the hadronic phase after the hadronization procedure. On the other side, it requires the interpretation of the EoS in terms of properties of degrees of freedom and their interactions: the QGP phase is modeled by interacting off-shell quasipartcles within the DQPM model which reproduces the lQCD thermodynamics near equilibrium and leads to a large and temperature dependent $\eta/s(T)$, which does not lead to a very early thermalization as assumed in the EPOS hydrodynamical expansion.

(3) The underestimation by EPOSir + PHSDe (similar to the PHSD) of the intermediate and high p_T range of hadron spectra and flow coefficients indicate that the initial space anisotropy—from the Pomeron breaking as in EPOS—is less developing into flow and anisotropic flow in the microscopic nonequilibrium dynamics of PHSD during the partonic and hadronic phases. All that leads to more soft spectra of EPOSir + PHSDe, which deviate form the experimental data with increasing p_T.

Thus, by developing EPOSir + PHSDe we obtain an interesting tool to investigate the different aspects of heavy-ion dynamics to optimize their modeling based on a solid theoretical ground.

ACKNOWLEDGMENTS

The authors thank J. Aichelin for useful discussions and valuable suggestions and to I. Karpenko for the guide to the details of hydrodinamical models. We are grateful to W. Cassing for a careful reading of the manuscript and important comments. We also acknowledge the support by the Deutsche Forschungsgemeinschaft (DFG, German Research Foundation) through Grant No. CRC-TR211 "Strong-interaction matter under extreme conditions" (Project No. 315477589-TRR 211).

DATA AVAILABILITY

The data that support the findings of this article are not publicly available. The data are available from the authors upon reasonable request.

[1] T. Hirano and M. Gyulassy, Nucl. Phys. A **769**, 71 (2006).
[2] E. Shuryak, Prog. Part. Nucl. Phys. **62**, 48 (2009).
[3] H. van Hees, V. Greco, and R. Rapp, Phys. Rev. C **73**, 034913 (2006).
[4] H. Song, S. A. Bass, U. Heinz, T. Hirano, and C. Shen, Phys. Rev. Lett. **106**, 192301 (2011); **109**, 139904(E) (2012).
[5] M. Asakawa, S. A. Bass, and B. Muller, Phys. Rev. Lett. **96**, 252301 (2006).
[6] J. Berges, K. Boguslavski, S. Schlichting, and R. Venugopalan, Phys. Rev. D **89**, 074011 (2014).
[7] A. Kurkela, A. Mazeliauskas, J.-F. Paquet, S. Schlichting, and D. Teaney, Phys. Rev. Lett. **122**, 122302 (2019).
[8] G. Giacalone, A. Mazeliauskas, and S. Schlichting, Phys. Rev. Lett. **123**, 262301 (2019).
[9] M. Greif, C. Greiner, B. Schenke, S. Schlichting, and Z. Xu, Nucl. Phys. A **982**, 491 (2019).
[10] Y. Xu, P. Moreau, T. Song, M. Nahrgang, S. A. Bass, and E. Bratkovskaya, Phys. Rev. C **96**, 024902 (2017).
[11] K. Werner, Phys. Rev. C **108**, 064903 (2023).
[12] K. Werner and B. Guiot, Phys. Rev. C **108**, 034904 (2023).
[13] K. Werner, Phys. Rev. C **109**, 034918 (2024).
[14] K. Werner, Phys. Rev. C **109**, 014910 (2024).
[15] K. Werner, arXiv:2410.09955.
[16] H. J. Drescher, M. Hladik, S. Ostapchenko, T. Pierog, and K. Werner, Phys. Rep. **350**, 93 (2001).
[17] K. Werner, Phys. Rev. Lett. **98**, 152301 (2007).
[18] K. Werner, I. Karpenko, T. Pierog, M. Bleicher, and K. Mikhailov, Phys. Rev. C **82**, 044904 (2010).
[19] K. Werner, B. Guiot, I. Karpenko, and T. Pierog, Phys. Rev. C **89**, 064903 (2014).
[20] W. Cassing and E. L. Bratkovskaya, Phys. Rev. C **78**, 034919 (2008).
[21] W. Cassing and E. L. Bratkovskaya, Nucl. Phys. A **831**, 215 (2009).
[22] W. Cassing, Eur. Phys. J. Spec. Top. **168**, 3 (2009).
[23] E. L. Bratkovskaya, W. Cassing, V. P. Konchakovski, and O. Linnyk, Nucl. Phys. A **856**, 162 (2011).
[24] V. P. Konchakovski, E. L. Bratkovskaya, W. Cassing, V. D. Toneev, and V. Voronyuk, Phys. Rev. C **85**, 011902 (2012).
[25] T. Song, H. Berrehrah, D. Cabrera, J. M. Torres-Rincon, L. Tolos, W. Cassing, and E. Bratkovskaya, Phys. Rev. C **92**, 014910 (2015).

[26] E. L. Bratkovskaya, A. Palmese, W. Cassing, E. Seifert, T. Steinert, and P. Moreau, J. Phys.: Conf. Ser. **878**, 012018 (2017).
[27] O. Linnyk, E. L. Bratkovskaya, and W. Cassing, Prog. Part. Nucl. Phys. **87**, 50 (2016).
[28] P. Moreau, O. Soloveva, L. Oliva, T. Song, W. Cassing, and E. Bratkovskaya, Phys. Rev. C **100**, 014911 (2019).
[29] M. Bleicher, *et al.*, J. Phys. G **25**, 1859 (1999).
[30] I. G. Bearden, *et al.* (BRAHMS Collaboration), Phys. Rev. Lett. **88**, 202301 (2002).
[31] W. Cassing and S. Juchem, Nucl. Phys. A **665**, 377 (2000).
[32] W. Cassing and S. Juchem, Nucl. Phys. A **672**, 417 (2000).
[33] L. P. Kadanoff and G. Baym, *Quantum Statistical Mechanics* (W. A. Benjamin, New York, NY, 1962).
[34] S. Juchem, W. Cassing, and C. Greiner, Nucl. Phys. A **743**, 92 (2004).
[35] W. Cassing, *Transport Theories for Strongly-Interacting Systems*, Lecture Notes in Physics Vol. 989 (Springer, Cham, 2021).
[36] B. Nilsson-Almqvist and E. Stenlund, Comput. Phys. Commun. **43**, 387 (1987).
[37] B. Andersson, G. Gustafson, and H. Pi, Z. Phys. C **57**, 485 (1993).
[38] T. Sjöstrand, S. Mrenna, and P. Z. Skands, J. High Energy Phys. 05 (2006) 026.
[39] V. Kireyeu, I. Grishmanovskii, V. Kolesnikov, V. Voronyuk, and E. Bratkovskaya, Eur. Phys. J. A **56**, 223 (2020).
[40] W. Cassing, A. Palmese, P. Moreau, and E. L. Bratkovskaya, Phys. Rev. C **93**, 014902 (2016).
[41] A. Palmese, W. Cassing, E. Seifert, T. Steinert, P. Moreau, and E. L. Bratkovskaya, Phys. Rev. C **94**, 044912 (2016).
[42] E. L. Bratkovskaya and W. Cassing, Nucl. Phys. A **807**, 214 (2008).
[43] T. Song, L. Tolos, J. Wirth, J. Aichelin, and E. Bratkovskaya, Phys. Rev. C **103**, 044901 (2021).
[44] W. Cassing and E. L. Bratkovskaya, Phys. Rep. **308**, 65 (1999).
[45] S. Borsanyi, J. N. Guenther, R. Kara, Z. Fodor, P. Parotto, A. Pasztor, C. Ratti, and K. K. Szabo, Phys. Rev. D **105**, 114504 (2022).
[46] W. Cassing, Nucl. Phys. A **791**, 365 (2007).
[47] W. Cassing, Nucl. Phys. A **795**, 70 (2007).
[48] O. Soloveva, P. Moreau, and E. Bratkovskaya, Phys. Rev. C **101**, 045203 (2020).
[49] Y. Aoki, S. Borsanyi, S. Durr, Z. Fodor, S. D. Katz, S. Krieg, and K. K. Szabo, J. High Energy Phys. 06 (2009) 088.
[50] M. Cheng, *et al.*, Phys. Rev. D **77**, 014511 (2008).
[51] J. A. Fotakis, O. Soloveva, C. Greiner, O. Kaczmarek, and E. Bratkovskaya, Phys. Rev. D **104**, 034014 (2021).
[52] O. Soloveva, P. Moreau, L. Oliva, V. Voronyuk, V. Kireyeu, T. Song, and E. Bratkovskaya, Particles **3**, 178 (2020).
[53] I. Grishmanovskii, O. Soloveva, T. Song, C. Greiner, and E. Bratkovskaya, Phys. Rev. C **109**, 024911 (2024).
[54] W. Cassing, L. Tolos, E. L. Bratkovskaya, and A. Ramos, Nucl. Phys. A **727**, 59 (2003).
[55] https://klaus.pages.in2p3.fr/epos4/pdf/eposParticleList.pdf.
[56] R. Marty, E. Bratkovskaya, W. Cassing, and J. Aichelin, Phys. Rev. C **92**, 015201 (2015).
[57] I. G. Bearden, *et al.* (BRAHMS Collaboration), Phys. Rev. Lett. **94**, 162301 (2005).
[58] I. G. Bearden, *et al.* (BRAHMS Collaboration), Phys. Rev. Lett. **93**, 102301 (2004).
[59] J. Adams, *et al.* (STAR Collaboration), Phys. Rev. Lett. **92**, 112301 (2004).
[60] B. B. Back, *et al.* (PHOBOS Collaboration), Phys. Lett. B **578**, 297 (2004).
[61] A. Adare, *et al.* (PHENIX Collaboration), Phys. Rev. C **88**, 024906 (2013).
[62] J. Adams, *et al.* (STAR Collaboration), Phys. Rev. Lett. **98**, 062301 (2007).
[63] V. P. Konchakovski, W. Cassing, and V. D. Toneev, J. Phys. G **42**, 055106 (2015).
[64] K. H. Ackermann, *et al.* (STAR Collaboration), Phys. Rev. Lett. **86**, 402 (2001).
[65] A. Adare, *et al.* (PHENIX Collaboration), Phys. Rev. C **93**, 051902 (2016).
[66] B. B. Back, *et al.* (PHOBOS Collaboration), Phys. Rev. C **72**, 051901 (2005).
[67] S. A. Voloshin, A. M. Poskanzer, A. Tang, and G. Wang, Phys. Lett. B **659**, 537 (2008).
[68] A. M. Poskanzer and S. A. Voloshin, Phys. Rev. C **58**, 1671 (1998).